Coastal Engineering 202 (2025) 104819

Contents lists available at ScienceDirect

Coastal Engineering

journal homepage: www.elsevier.com/locate/coastaleng

REEF3D::NHFLOW—A high-performance non-hydrostatic solver for coastal wave propagation

Hans Bihs *, Widar Weizhi Wang

Department of Civil and Environmental Engineering, Norwegian University of Science and Technology (NTNU), Høgskoleringen 7A, 7491 Trondheim, Norway

ARTICLE INFO

Keywords:
Non-hydrostatic modeling
Coastal wave modeling
Varying bathymetry
Irregular coastline
REEF3D

ABSTRACT

In this paper the new three-dimensional non-hydrostatic wave model NHFLOW is presented. It solves the non-hydrostatic Euler equations on a σ-coordinate grid, which follows the free surface and bottom topography, allowing for grid refinement near the water surface. The governing equations are treated with a Godunov-type scheme. A pressure correction algorithm is implemented, which results in excellent dispersion properties. Together, this delivers a unique combination of shock-capturing properties and dispersive wave modeling capabilities. The structure of the coefficient matrix of the Poisson equation is simplified through a deferred correction approach, increasing the iterative solver's performance significantly. In order to model propagating waves with a high level of accuracy, the numerical fluxes are reconstructed with the fifth-order WENO scheme. Developed within the open-source hydrodynamic framework REEF3D, the new model is fully parallelized and utilizes the domain decomposition strategy with MPI communication between processors. This paper showcases the capabilities of this new and efficient non-hydrostatic model through verification and validation with a range of laboratory and real-world wave propagation cases.

1. Introduction

The simulation of wave propagation from offshore areas towards the coast is a critical part of many marine engineering applications. Over the last decades, rapid advances have been achieved in the field of phase-resolved wave modeling, which helps to resolve wave diffraction, refraction, shoaling and breaking of waves. Boussinesq wave models are a class of depth-averaged models based on the shallow water equations (SWE) that include terms to represent the effect of the non-hydrostatic pressure explicitly. Based on earlier versions of the Boussinesq equations (e.g. Peregrine (1967) or Svendsen (1974)), Madsen et al. (1991) and Nwogu (1993) proposed in two separate approaches new forms that improved the dispersion characteristics significantly. Several researchers have extended the Boussinesq equations to higher-order to extend their validity to deeper water depths, see e.g. Fuhrman and Bingham (2004) or Madsen et al. (2002). Independent of each other, Shi et al. (2023) and Roeber et al. (2010) have reformulated the Boussinesq equations in conservative form and used shock-absorbing discretization techniques in their respective models. Today, several open-source Boussinesq models exist, such as FUNWAVE (Wei et al., 1995) or COULWAVE (Lynnett et al., 2002) that have been widely used for coastal engineering applications. Another way to use the shallow water equations for wave propagation calculation is to solve for the non-hydrostatic pressure in order to represent its effect on the vertical velocity. Stelling and Zijlema (2003) introduced this approach, which was later updated by the work of Zijlema and Stelling (2005). Here, the velocities are computed on a staggered mesh, and the pressure is found through a projection-type method with Keller-box configuration. The pressure is assumed to vary linearly over the water depth. Their methods resulted in the depth-averaged version of the open-source model SWASH (Zijlema et al., 2011). This approach is similarly implemented in XBeach (Roelvink et al., 2009), which is widely used for calculating coastal erosion processes (Smit et al., 2010). Jeschke et al. (2017) extended the non-hydrostatic SWE approach to include a quadratic pressure variation over the water depth, leading to improved dispersion characteristics. This approach was later included in the SFLOW module of the open-source hydrodynamic framework REEF3D (Wang et al., 2020b) where it was adapted for varying bathymetry. Overall, run-up of waves can be easily included in SWE-based models through a wetting and drying algorithm (e.g. Roeber and Cheung (2012) or Zijlema et al. (2011)), while the water depth remains an inherent limitation to varying degrees for all models based on the SWE.

One way to overcome this problem is to employ the potential flow approach. Solving the fully nonlinear potential flow equations, Grilli et al. (1989) used the boundary-element method to calculate propagating waves for coastal problems. This approach was later extended

* Corresponding author.
E-mail addresses: hans.bihs@ntnu.no (H. Bihs), widar.w.wang@ntnu.no (W.W. Wang).

https://doi.org/10.1016/j.coastaleng.2025.104819
Received 17 February 2025; Received in revised form 1 July 2025; Accepted 2 July 2025
Available online 26 July 2025

to capture breaking waves (Grilli et al., 2001). Li and Fleming (1997) solved the Laplace equation for the velocity potential using a finite difference method and a multigrid solver together with the dynamic and kinematic free surface boundary conditions. Bingham and Zhang (2007) extended this approach to include arbitrary-order finite difference schemes. The work of Engsig-Karup et al. (2009) further extended this method to three dimensions and added a GMRES iterative solver to the multigrid preconditioning. The resulting OceanWave3D model is published as open-source and additional work resulted in applications to wave-structure-interaction (Ducrozet et al., 2010) or ship hydrodynamics (Afshar and Bingham, 2017). A GPU parallelized version of OceanWave3D is available as well (Engsig-Karup et al., 2012). Fully nonlinear potential flow using finite difference methods is also the basis for REEF3D::FNPF (Bihs et al., 2019). Here, a relatively straightforward approach to include coastlines was introduced (Wang et al., 2022a) without the need to body-fit the grid to the wet-dry interface. The model has also been used to generate deep water waves for the design of offshore structures (Wang et al., 2021), including the nonlinear wave kinematics for rapid wave load calculation (Pakozdi et al., 2022). High-order spectral (HOS) (Ducrozet et al., 2012) is yet another modeling approach based on potential flow, but due to the numerical methods involved, it is generally used for water wave propagation excluding effects of bathymetry variations or coastlines.

A limitation of potential flow based models is the fact that the flow is irrotational and inviscid, which makes it difficult to capture crucial coastal processes such as sediment transport. Also, run-up through a wetting and drying algorithm remains a challenge and has mostly been excluded from such type of models. The solution of the Navier–Stokes equation resolves most of the wave hydrodynamic processes. Examples are the waves2foam library (Jacobsen et al., 2012) for the open-source computational fluid dynamics (CFD) model OpenFOAM, OlaFlow (Higuera et al., 2013) or REEF3D::CFD (Bihs et al., 2016). But because this comes at the cost of significant computational resources, the application of CFD models for waves is mostly limited to the near-field hydrodynamics around structures (Aggarwal et al., 2019) or when processes like breaking waves need to be captured with high levels of detail (Larsen and Fuhrman, 2018). On the other hand, Casulli and Stelling (1998) demonstrated in one of the early attempts to employ Navier–Stokes equations for wave propagation problems the potential for efficient computation. Using a fractional step solution algorithm, they successfully captured frequency dispersion by solving for the non-hydrostatic pressure. At that stage, validating wave transformation over a submerged bar still required a relatively high number of 32 vertical elements. Several authors presented non-hydrostatic wave models using σ-coordinate grids (Stelling and Zijlema, 2003)(Lin and Li, 2002)(Li, 2008). The three-dimensional version of SWASH (Zijlema et al., 2011) effectively reduced the number of required vertical layers while still accurately capturing wave dispersion. For wave propagation over the submerged bar case by Ohyama et al. (1995), only two vertical layers were needed. This is made possible by the Keller-box scheme, which places the non-hydrostatic pressure directly on the free surface, i.e. the top grid line. In addition, Zijlema and Stelling (2005) showed that their pressure correction scheme was superior over standard projection methods for the non-hydrostatic pressure solution. For wave breaking, SWASH locally turns off the non-hydrostatic pressure and resorts to the hydrostatic solution. Whereas this model used a staggered mesh for the location of the velocities, Ma et al. (2012) introduced the non-hydrostatic NHWAVE that uses a Godunov-type scheme with velocities placed at the cell centers. Here, the non-hydrostatic pressure is located at the vertical cell faces in order to fulfill the zero boundary condition at the free surface directly. For the solution of the non-hydrostatic pressure, the projection method is used. NHWAVE's governing equations are formulated similar to the conservative SWE. Together with the numerical scheme for the fluxes, this results in both conservative and shock-capturing characteristics, obviating the need for a dedicated breaking wave model. The model has been used for several coastal engineering applications, such as for example tsunami waves generated by submarine landslides (Ma et al., 2013), modeling of porous structures (Ma et al., 2014) and wave-structure interaction (Ma et al., 2016).

The current paper presents the new non-hydrostatic wave model NHFLOW, which is part of the REEF3D framework (Wang et al., 2020a). The model follows NHWAVE's numerical approach for the spatial discretization and uses a Godunov-type scheme and the HLL Riemann approximation for calculating the fluxes at the cell faces in order to achieve shock-capturing properties. For the solution of the non-hydrostatic pressure, the new model follows SWASH's concept of the pressure correction method. The new model NHFLOW delivers improvements in several key aspects, which are documented in the current paper through a range of validation test cases:

- The numerical fluxes for the approximate HLL Riemann solver are reconstructed with the fifth-order WENO (weighted essentially non-oscillatory) scheme (Jiang and Shu, 1996), resulting in high levels of numerical accuracy and stability.
- Similar to SWASH, the new model NHFLOW uses a pressure correction scheme for the non-hydrostatic pressure. This modification leads to significantly improved wave dispersion over the standard pressure projection method.
- By utilizing the deferred correction approach (Peric and Ferziger, 2001), the complexity of the matrix for the discretized pressure correction Poisson equation on a σ-grid is reduced. This leads to significantly faster solutions when using the conjugate gradient solver with geometric multigrid preconditioning.

As part of the REEF3D framework, NHFLOW further benefits from its high-performance capabilities and access to the hypre solvers (Ashby and Falgout, 1996). Mesh generation, bathymetry, geometry handling, and post-processing remain consistent with REEF3D's other solvers. Additionally, similar to the hydrodynamic coupling between REEF3D's FNPF and CFD (Wang et al., 2022b; Kamath et al., 2023), NHFLOW also supports coupling with CFD. The following sections detail NHFLOW's numerical approach, followed by model validation against relevant experimental data. The results demonstrate NHFLOW's ability to accurately model dispersive wave transformation. Finally, the model's high-performance capabilities are evaluated using a real-world wave scenario.

2. Numerical model

2.1. Governing equations

The model REEF3D::NHFLOW solves the continuity, the free surface and the three-dimensional Euler equations in the following format. Here, the indices are defined as (i,j) = 1,2,3 so that for three spatial dimensions $x_1 = x$, $x_2 = y$, and $x_3 = z$. The definition of the water depth $h(x,y,t) = \eta(x,y,t) + d(x,y)$, where $\eta(x,y,t)$ is the free surface elevation and $d(x,y)$ stretches from the bed to the still water level.

$$\frac{\partial u_i}{\partial x_i} = 0 \tag{1}$$

$$\frac{\partial hu_i}{\partial t} + u_j \frac{\partial hu_i}{\partial x_j} = -\frac{h}{\rho}\frac{\partial p}{\partial x_i} - hg_i \tag{2}$$

In the current paper, the focus is on pure wave propagation problems, thus the influence of the viscosity is neglected. Extending the code to capture viscous flow is straightforward by including the viscous stresses in Eq. (2). The changes of the dynamic free surface are solved by integrating the horizontal velocity fluxes over the water depth where h remains the single-valued water depth in the horizontal plane:

$$\frac{\partial h}{\partial t} + \frac{\partial}{\partial x_i}\int_{-d}^{\eta} hu_i \, dz = 0 \tag{3}$$

The one-phase flow model selects the efficient approach of a free surface and bottom following σ-grid (Li and Fleming, 1997). The z-coordinate in the vertical direction is then transformed with the following expression:

$$\sigma = \frac{z + d(x,y)}{h(x,y,t)} \tag{4}$$

The σ-coordinate system is both bathymetry and free surface following, thus the terms for the σ-coordinate transformation can be calculated as follows (Madsen, 2009):

$$\begin{aligned}
\frac{\partial \sigma}{\partial t} &= -\frac{\sigma}{h}\frac{\partial h}{\partial t} \\
\frac{\partial \sigma}{\partial x} &= (1-\sigma)\frac{1}{h}\frac{\partial d}{\partial x} - \sigma\frac{1}{h}\frac{\partial \eta}{\partial x} \\
\frac{\partial \sigma}{\partial y} &= (1-\sigma)\frac{1}{h}\frac{\partial d}{\partial y} - \sigma\frac{1}{h}\frac{\partial \eta}{\partial y} \\
\frac{\partial \sigma}{\partial z} &= \frac{1}{h}
\end{aligned} \tag{5}$$

The governing momentum equations including the temporal, convection and source terms can be written in vector form:

$$\frac{\partial \mathbf{U}}{\partial t} + \frac{\partial \mathbf{F(U)}}{\partial x} + \frac{\partial \mathbf{G(U)}}{\partial y} + \frac{\partial \mathbf{H(U)}}{\partial \sigma} = \mathbf{S} \tag{6}$$

Here, $U = (hu, hv, hw)^{\intercal}$. Following the concept of the conservative shallow water equations (see e.g. Roeber et al. (2010) or Ma et al. (2012)), the individual vector components can be written as follows:

$$\mathbf{F} = \begin{bmatrix} hu^2 + \frac{1}{2}g\eta^2 + g\eta d \\ huv \\ huw \end{bmatrix} \quad \mathbf{G} = \begin{bmatrix} huv \\ hv^2 + \frac{1}{2}g\eta^2 + g\eta d \\ hvw \end{bmatrix} \quad \mathbf{H} = \begin{bmatrix} u\omega \\ v\omega \\ w\omega \end{bmatrix} \tag{7}$$

The source term vectors contain the bed gradient term from the hydrostatic pressure gradient splitting (Liang and Marche, 2009) as well as the non-hydrostatic pressure gradient.

$$\mathbf{S} = \begin{bmatrix} g\eta\frac{\partial d}{\partial x} - \frac{h}{\rho}\left(\frac{\partial p}{\partial x} + \frac{\partial p}{\partial \sigma}\frac{\partial \sigma}{\partial x}\right) \\ g\eta\frac{\partial d}{\partial y} - \frac{h}{\rho}\left(\frac{\partial p}{\partial y} + \frac{\partial p}{\partial \sigma}\frac{\partial \sigma}{\partial y}\right) \\ -\frac{h}{\rho}\frac{\partial p}{\partial \sigma}\frac{\partial \sigma}{\partial z} \end{bmatrix} \tag{8}$$

The relative vertical velocity ω in the σ-coordinate frame replaces the vertical velocity w in the governing equations. This way, the σ-transformation terms are included in the convection discretization without the need to add them explicitly. The relative vertical velocity ω is defined as:

$$\omega = h\left(\frac{\partial \sigma}{\partial t} + u\frac{\partial \sigma}{\partial x} + v\frac{\partial \sigma}{\partial y} + w\frac{\partial \sigma}{\partial z}\right) \tag{9}$$

2.2. Spacial discretization

The spatial discretization of the conservative variables h, hu, hv and hw is crucial for achieving stable and accurate numerical behavior. The conserved variables are located at the cell center. For example, the contribution from the change of the numerical flux $\mathbf{F(U)}$ in x-direction from Eq. (6) can be estimated by computing the conservative flux difference from the cell faces $i+1/2$ and $i-1/2$:

$$\frac{\partial \mathbf{F(U)}}{\partial x} \approx \frac{\mathbf{F}(\mathbf{U}^-, \mathbf{U}^+)_{i+1/2} - \mathbf{F}(\mathbf{U}^-, \mathbf{U}^+)_{i-1/2}}{\Delta x} \tag{10}$$

A Godunov-type scheme is employed to approximate the numerical fluxes at the cell faces. In the following, the procedure is given in the context of the treatment of the numerical flux $\mathbf{F(U)}$ at the cell face $i+1/2$ and the reconstructed velocity in x-direction, i.e. the left value $\mathbf{U}^-$ and the right value $\mathbf{U}^+$. The $\mathbf{U}^{\pm}$ are reconstructed at the cell faces using the 5th-order WENO scheme (Jiang and Shu, 1996). The terms U^1, U^2 and U^3 represent the three ENO stencils which are weighted according to the smoothness of the solution in each of the stencils.

$$\mathbf{U_{i+1/2}}^{\pm} = \omega_1^{\pm} U_{i+1/2}^{1\pm} + \omega_2^{\pm} U_{i+1/2}^{2\pm} + \omega_3^{\pm} U_{i+1/2}^{3\pm} \tag{11}$$

The ENO stencils are defined as:

$$\begin{aligned}
U_{i+1/2}^{1\pm} &= \frac{1}{3}q_1^{\pm} - \frac{7}{6}q_2^{\pm} + \frac{11}{6}q_3^{\pm}, \\
U_{i+1/2}^{2\pm} &= -\frac{1}{6}q_2^{\pm} + \frac{5}{6}q_3^{\pm} + \frac{1}{3}q_4^{\pm}, \\
U_{i+1/2}^{3\pm} &= \frac{1}{3}q_3^{\pm} + \frac{5}{6}q_4^{\pm} - \frac{1}{6}q_5^{\pm}
\end{aligned} \tag{12}$$

The weights $\omega_i\pm$ are determined based on the smoothness of the solution as outlined in Jiang and Shu (1996):

$$\omega_1^{\pm} = \frac{\alpha_1^{\pm}}{\alpha_1^{\pm} + \alpha_2^{\pm} + \alpha_3^{\pm}}, \quad \omega_2^{\pm} = \frac{\alpha_2^{\pm}}{\alpha_1^{\pm} + \alpha_2^{\pm} + \alpha_3^{\pm}}, \quad \omega_3^{\pm} = \frac{\alpha_3^{\pm}}{\alpha_1^{\pm} + \alpha_2^{\pm} + \alpha_3^{\pm}}, \tag{13}$$

and

$$\alpha_1^{\pm} = \frac{1}{10}\frac{1}{\left(\widetilde{\epsilon} + IS_1^{\pm}\right)^2}, \quad \alpha_2^{\pm} = \frac{6}{10}\frac{1}{\left(\widetilde{\epsilon} + IS_2^{\pm}\right)^2}, \quad \alpha_3^{\pm} = \frac{3}{10}\frac{1}{\left(\widetilde{\epsilon} + IS_3^{\pm}\right)^2} \tag{14}$$

The regularization parameter $\widetilde{\epsilon} = 10^{-6}$ avoids division by zero and the smoothness indicators $IS\pm$ are calculated as:

$$\begin{aligned}
IS_1^{\pm} &= \frac{13}{12}\left(q_1^{\pm} - 2q_2^{\pm} + q_3^{\pm}\right)^2 + \frac{1}{4}\left(q_1^{\pm} - 4q_2^{\pm} + 3q_3^{\pm}\right)^2, \\
IS_2^{\pm} &= \frac{13}{12}\left(q_2^{\pm} - 2q_3^{\pm} + q_4^{\pm}\right)^2 + \frac{1}{4}\left(q_2^{\pm} - q_4^{\pm}\right)^2, \\
IS_3^{\pm} &= \frac{13}{12}\left(q_3^{\pm} - 2q_4^{\pm} + q_5^{\pm}\right)^2 + \frac{1}{4}\left(3q_3^{\pm} - 4q_4^{\pm} + q_5^{\pm}\right)^2
\end{aligned} \tag{15}$$

Finally, the q-values for the left and right sides are defined as:

$$\begin{aligned}
q_1^- &= u_{i-2},\ q_2^- = u_{i-1},\ q_3^- = u_i,\ q_4^- = u_{i+1},\ q_5^- = u_{i+2} \\
q_1^+ &= u_{i+3},\ q_2^+ = u_{i+2},\ q_3^+ = u_{i+1},\ q_4^+ = u_i,\ q_5^+ = u_{i-1}
\end{aligned} \tag{16}$$

Stencils with a smoother solution receive larger weights, whereas the influence of stencils with discontinuous solutions is reduced. The resulting scheme reconstructs the fluxes with 5th-order accuracy, which is reduced to 3rd-order in case of discontinuities. As the WENO scheme is free of limiters, it maintains the solution's sharpness of discontinuities and extreme values.

With the reconstructed face values $\mathbf{U}^-$ and $\mathbf{U}^+$, the horizontal flux $\mathbf{F}(\mathbf{U}^-, \mathbf{U}^+)$ at the cell face is approximated with the HLL Riemann solver (Harten et al., 1983):

$$\mathbf{F}(\mathbf{U}^-, \mathbf{U}^+) = \begin{cases} \mathbf{F}(\mathbf{U}^-) & if\ s^- \geq 0 \\ \mathbf{F}^*(\mathbf{U}^-, \mathbf{U}^+) & if\ s^- < 0 < s^+ \\ \mathbf{F}(\mathbf{U}^+) & if\ s^+ \leq 0 \end{cases} \tag{17}$$

with

$$\mathbf{F}^*(\mathbf{U}^-, \mathbf{U}^+) = \frac{s^+\mathbf{F}(\mathbf{U}^-) - s^-\mathbf{F}(\mathbf{U}^+) + s^-s^+\left(\mathbf{U}^+ - \mathbf{U}^-\right)}{s^+ - s^-} \tag{18}$$

The left and right signal speeds are defined based on the horizontal velocity and the shallow water wave speed (see e.g. Shi et al. (2023) or Ma et al. (2012)):

$$\begin{aligned}
s^- &= MIN(\mathbf{U}^- - \sqrt{g\mathbf{H}^-}, \mathbf{U}^* - \sqrt{g\mathbf{H}^*}) \\
s^+ &= MAX(\mathbf{U}^+ + \sqrt{g\mathbf{H}^+}, \mathbf{U}^* + \sqrt{g\mathbf{H}^*})
\end{aligned} \tag{19}$$

The values $\mathbf{H}^{\pm}$ are the left and right water depth values reconstructed with the WENO scheme. The parameters $\mathbf{U}^*$ and $\sqrt{g\mathbf{H}^*}$ are given by:

$$\begin{aligned}
\mathbf{U}^* &= \frac{\mathbf{U}^- + \mathbf{U}^+}{2} + \sqrt{g\mathbf{H}^-} - \sqrt{g\mathbf{H}^+} \\
\sqrt{g\mathbf{H}^*} &= \frac{\sqrt{g\mathbf{H}^-} + \sqrt{g\mathbf{H}^+}}{2} + \frac{\mathbf{U}^- - \mathbf{U}^+}{4}
\end{aligned} \tag{20}$$

2.3. Time advancement scheme

The velocities and the free surface are advanced in time with a second-order TVD Runge–Kutta scheme (Gottlieb and Shu, 1998):

$$u_i^{(1)} = u_i^n + \Delta t L\left(u_i^n\right)$$
$$u_i^{n+1} = \frac{1}{2}u_i^n + \frac{1}{2}u_i^{(1)} + \frac{1}{2}\Delta t L\left(u_i^{(1)}\right) \tag{21}$$

The operator L contains all spatial discretizations of the governing equations and needs to be evaluated at each Runge–Kutta sub-step. For the time step size, adaptive time stepping using the Courant–Friedrichs–Lewy (CFL) criterion based on the shallow water wave speed and the maximal component-wise flow velocities is used:

$$\Delta t = CFL \cdot MIN\left[\frac{\Delta x_i}{|u_i| + \sqrt{gh}}\right] \tag{22}$$

2.4. Non-hydrostatic pressure solution

In the current implementation, the non-hydrostatic pressure is solved with a projection-based pressure correction algorithm (Chorin, 1968). As reported by Zijlema and Stelling (2005), the pressure correction approach is very suitable in terms of non-hydrostatic wave models and leads to significantly improved wave dispersion over the standard projection method. In effect, a predictor–corrector scheme, this method adds the gradient of the pressure p^n from the previous time step to the source terms of the momentum equations, see Eq. (8). After the solution of the intermediate velocity field, the pressure for the new time step p^{n+1} is updated with the pressure correction p':

$$p^{n+1} = p^n + p' \tag{23}$$

In terms of the σ-coordinate approach, the Poisson equation for the pressure correction p' with the continuity formulation for the velocities on the right-hand side reads as follows:

$$\begin{aligned}&\frac{\partial^2 p'}{\partial x^2} + \frac{\partial^2 p'}{\partial y^2} + \frac{\partial^2 p'}{\partial \sigma^2}\left[\left(\frac{\partial \sigma}{\partial x}\right)^2 + \left(\frac{\partial \sigma}{\partial y}\right)^2 + \left(\frac{\partial \sigma}{\partial z}\right)^2\right]\\ &+ \frac{\partial p'}{\partial \sigma}\left[\frac{\partial^2 \sigma}{\partial x^2} + \frac{\partial^2 \sigma}{\partial y^2}\right] + 2\left[\frac{\partial \sigma}{\partial x}\frac{\partial^2 p'}{\partial x \partial \sigma} + \frac{\partial \sigma}{\partial y}\frac{\partial^2 p'}{\partial y \partial \sigma}\right]\\ &= \frac{\rho}{\Delta t}\left[\frac{\partial u}{\partial x} + \frac{\partial u}{\partial \sigma}\frac{\partial \sigma}{\partial x} + \frac{\partial v}{\partial y} + \frac{\partial v}{\partial \sigma}\frac{\partial \sigma}{\partial y} + \frac{\partial w}{\partial \sigma}\frac{\partial \sigma}{\partial z}\right]\end{aligned} \tag{24}$$

The challenge with the Poisson equation on a σ-coordinate grid is the fact that it contains cross derivative terms associated with the grid transformation operators. In three dimensions, this results in a 15-point discretization stencil that contains the diagonal neighbor cells. By employing the deferred correction approach (Peric and Ferziger, 2001), i.e. moving the cross-derivative terms to the right-hand side of the system of linear equations, the stencil is reduced to 7-points. This leads to significant efficiency gains when solving the Poisson equation with hypre's conjugated gradient solver BiCGSTAB (van der Vorst, 1992) together with geometric multigrid preconditioner PFMG (Ashby and Falgout, 1996) without impeding numerical accuracy. In the following, the intermediate velocities u_i^* are corrected to make them divergence-free:

$$u^{n+1} = u^* - \frac{\Delta t}{\rho}\left(\frac{\partial p'}{\partial x} + \frac{\partial p'}{\partial \sigma}\frac{\partial \sigma}{\partial x}\right)$$
$$v^{n+1} = v^* - \frac{\Delta t}{\rho}\left(\frac{\partial p'}{\partial y} + \frac{\partial p'}{\partial \sigma}\frac{\partial \sigma}{\partial y}\right) \tag{25}$$
$$w^{n+1} = w^* - \frac{\Delta t}{\rho}\left(\frac{\partial p'}{\partial \sigma}\frac{\partial \sigma}{\partial z}\right)$$

2.5. Numerical implementations for coastal waves

A wetting and drying algorithm captures the dynamically moving wet-dry interface, see e.g. Roeber and Cheung (2012)(Ma et al., 2012). A minimum water depth h_{min} is maintained throughout the domain, and a cell becomes dry when it falls below this limit. A dry cell will become a wet cell when its free surface elevation η is lower than that of neighboring wet cells. Due to the shock-capturing characteristics of the Godunov-type scheme, the model runs stably. The model is fully parallelized using the domain decomposition approach and MPI. As shown in Section 4.2, it is possible to efficiently run the model in a highly parallelized fashion on supercomputer facilities. Waves can be generated (Jacobsen et al., 2012) and absorbed (Chen et al., 2019) with relaxation zones or alternatively with actively absorbing Dirichlet inlets and outlets (Higuera et al., 2013). The relaxation function used in the model is elaborated as follows:

$$\Gamma(\widetilde{x}) = 1 - \frac{e^{(\widetilde{x}^{3.5})} - 1}{e - 1} \; for \; \widetilde{x} \in [0; 1] \tag{26}$$

where $\widetilde{x}$ is scaled to the length of the relaxation zone, the water depth h, velocity u, uh and surface elevation η are increased to the analytical values in the wave generation zone following the relaxation function. A reverse process takes place in the wave absorption boundary.

3. Verification and validation

This section examines the new non-hydrostatic wave model for its capability of representing deep to shallow water waves and validates the model against experiments representing various coastal wave transformations.

3.1. Dispersion relation

As mentioned in Section 2.1, the proposed model operates on a surface and bottom-following σ-grid in the vertical direction. The number of vertical cells and the strength of the clustering towards the free surface both influence the representation of the dispersion relation of progressive waves. A linear regular wave with a wave height of 0.01 m and a wavelength of 6.2832 m (about 2π) is simulated over a wide range of constant water depth from 0.1 m to 100.0 m, which corresponds to $kd = 0.1 \sim 100$, where k is the wave number and d is the still water depth. The ratio between the simulated phase velocity c_n and the theoretical phase velocity c_t is used to evaluate the numerical representation of the dispersion relation at different kd. In the post-processing, the scenarios with kd values of 0.1 and 0.2 are excluded as these scenarios lead to shallow water nonlinear waves that are not comparable with the rest of the linear wave conditions. A convergence study shows that about 40 cells per wavelength can sufficiently represent the free surface. As a result, the horizontal cell size $dx = 0.15$ m is used for all cases together with an adaptive time step governed by $CFL = 0.5$. Each simulation is performed for 100 s, corresponding to about 50 wave periods for most of the scenarios. The domain length in the x-direction for the two-dimensional numerical wave tanks is 150 m, corresponding to about 24 wavelengths. A one-wavelength relaxation zone is used to generate the waves from the left-hand side inlet boundary, and a two-wavelength relaxation zone is placed at the right-hand side outlet boundary to minimize wave reflection. This leaves more than 20 wavelengths for the wave propagation. The wave gauge located at 10 wavelengths downstream is used for evaluating the phase velocity. The model is firstly tested using a uniform σ-grid in the vertical direction with different cell counts 1, 2, 3 and 5. The resulting phase-velocity ratios are plotted over kd as seen in Fig. 1(a). The model is able to represent the dispersion relation in deeper water with an increasing number of vertical cells. The accuracy of the phase velocity is maintained within 0.1% up to $kd = 40$ with 5 vertical cells. Different stretching factors α are also investigated while keeping

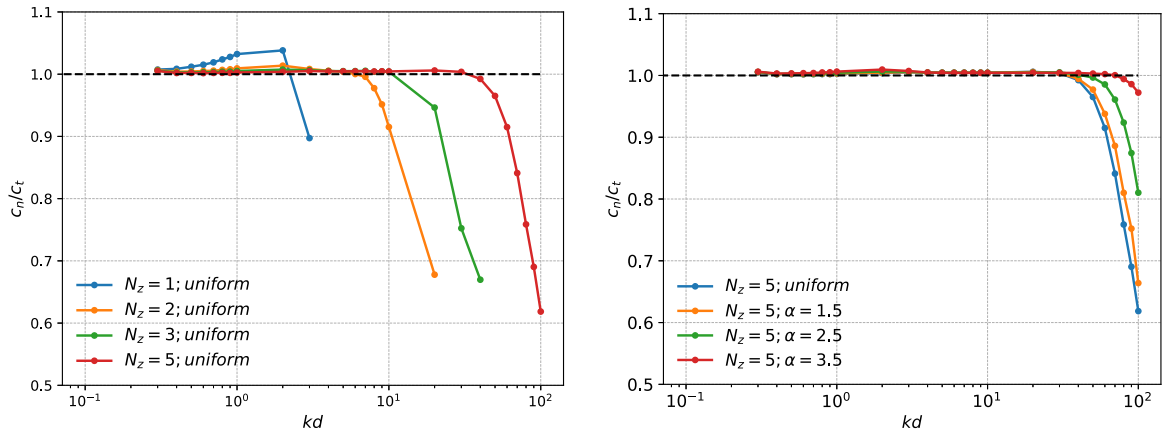

(a) Uniform vertical grid arrangement (b) Vertical grid with stretching

Fig. 1. Ratio of the simulated regular wave phase velocity to the theoretical phase velocity for different water depth conditions and vertical grid arrangements in REEF3D::NHFLOW.

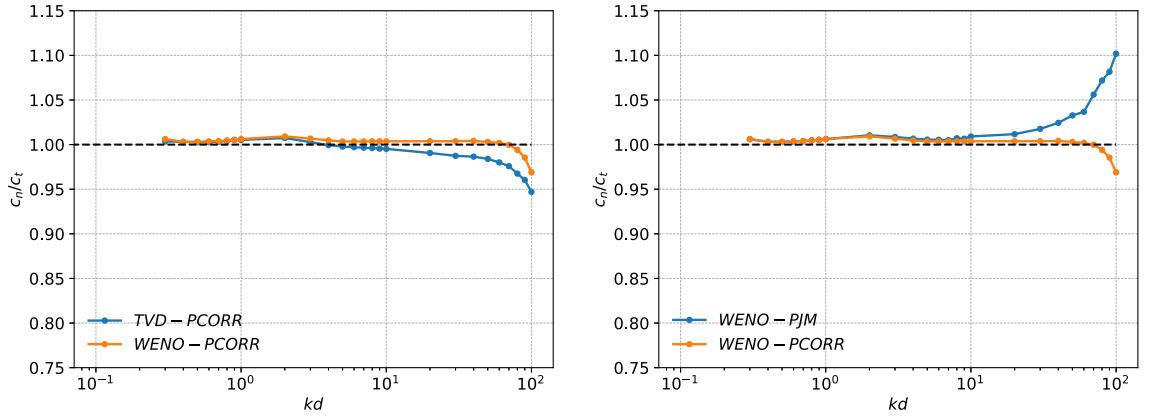

(a) Comparing WENO-PCORR with TVD-PCORR (b) Comparing WENO-PCORR with WENO-PJM

Fig. 2. Relative wave phase velocity with increasing water depth produced with the proposed combination of WENO-PCORR in comparison to (a) TVD-PCORR and (b) WENO-PJM.

5 vertical cells and the resulting phase-velocity ratios are shown in Fig. 1(b). The higher value of α indicates a stronger grid clustering towards the free surface. It is seen that a stronger clustering gives a better representation of the dispersion relation in deep water. A stretching factor of 3.5 enables the model to calculate the phase velocity within an accuracy of 0.1% up to $kd = 80$ using only 5 vertical cells. This shows that the model is capable of dispersive wave simulations over a wide range of water depths that are relevant for coastal engineering applications.

The simulations are conducted using the WENO flux reconstruction method in combination with the pressure correction scheme (PCORR), as detailed in Sections 2.2 and 2.4. For comparison, the relative phase velocity results are evaluated against those obtained using a second-order TVD flux reconstruction with the van Leer limiter (Ma et al., 2012) and the projection method (PJM). All simulations are carried out using a vertical discretization of five cells and a stretching factor of 3.5. The comparative results are presented in Fig. 2. An evident advantage of the proposed numerical implementations can be observed in relatively deeper water with $kd > 10$. The relative phase velocity values for all cases are summarized in Appendix.

3.2. Wave shoaling and decomposition

Water depth variations in the coastal area lead to a series of wave transformations. To examine the model's capability of representing the various wave transformations, the model is firstly validated against the experiment by Beji and Battjes (1993) for wave shoaling and decomposition over a submerged bar. Linear waves with a wave height $H = 0.02$ m and a wave period of $T = 2.02$ s are generated. The waves propagate towards the front slope of the submerged bar with a slope of 1:20, where the waves shoal but do not break. On top of the bar and on the 1:10 downward-directed slope, the waves are decomposed into their higher-order harmonics. This feature makes the submerged bar experiment a highly relevant test case for testing the dispersion capabilities of the wave model, as relatively short waves with large kd values are generated. The experimental setup and the locations of the 8 wave gages are shown in Fig. 3.

The numerical model uses 1200 cells in the x-direction and 3 vertical layers with exponential stretching towards the free surface (exponential stretching factor 2.5). A CFL number of 1.0 is used to determine the time step size. The simulation is run for $T = 60$ s, which takes ca. 17.5s on a MacBook Pro with an M3 Max chip and 12 performance cores. The simulated free surface elevation time series at all wave gages are compared to the experimental measurements in Fig. 4. After the waves have passed the submerged bar, higher-order harmonics are formed that result in highly dispersive waves. Overall, the model maintains the wave amplitudes and phase well throughout the wave tank compared to the measurements. The results demonstrate the capability to simulate complex wave transformation over a varying bed topography with a relatively coarse mesh.

As a baseline, all of the cases simulated in the current paper are simulated with 5th-order WENO flux reconstruction, see Section 2.2.

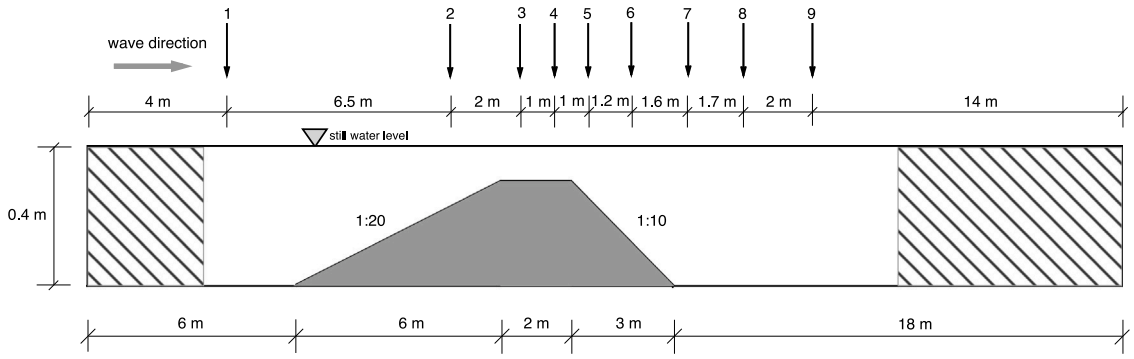

Fig. 3. Wave gage placement for the submerged bar test case.

In order to show its effectiveness, the submerged bar is rerun with the 2nd-order TVD flux reconstruction with van Leer limiter (see e.g. Ma et al. (2012)). The comparison in Fig. 5 shows that the WENO scheme maintains the wave elevation correctly until the last wave gage 9, whereas significant wave damping can be observed for the TVD scheme for the same grid resolution. Fig. 6 shows the performance of the projection method against the pressure correction method. The results also show a reduction in wave elevation for the projection method, this time due to the inability to capture all frequencies accurately with 3 vertical layers.

The worst performance for the given mesh configuration is delivered by the combination of the TVD flux reconstruction and the projection method (PJM), as can be seen in Fig. 7. On a Macbook Pro with the 12-performance-core M4 Max, the TVD+PJM simulation takes $14.2s$ to reach $60s$ simulated waves, where as the basline WENO+PCORR simulation takes only slightly longer with $15.8s$. Generally, it can be expected that the results with the TVD scheme will improve with an increased number of horizontal cells. For the projection method, dispersion will be improved with a larger number of vertical cells.

3.3. Wave shoaling and refraction

Three-dimensional water depth variations often lead to wave refraction in addition to shoaling. The experiment of Whalin (1971) investigates wave shoaling and refraction over a semi-circular submerged reef. The proposed non-hydrostatic model is validated against the experimental data in this section. The schematics of the numerical wave tank follow the physical experiment configurations and can be seen in Fig. 8. The semi-circular slope starts 7.62 m from the inlet boundary to the left-hand side and rises to 0.305 m over a horizontal distance of 7.62 m. The still water depth at the left-hand side boundary is 0.457 m. An array of 39 wave gages are arranged between $x = 3.505$ m and 22.551 m. The coordinates of the gages are summarized in Table 1. A second-order Stokes wave with a wave height of 0.015 m and a wave period of 2.0 s is generated at the left-hand side using a relaxation zone of 5 m, around one wavelength. Another relaxation zone of 10 m is applied to the outlet boundary on the right-hand side to act as a numerical beach and minimize undesired wave reflection. A grid convergence study leads to 0.05 m horizontal cell size. Five uniform vertical cells are used based on the intermediate water depth at the wave generation boundary with $kd = 0.74$. The CFL number of 0.5 is used. The wave propagation is simulated for 100 s, corresponding to about 50 wave periods.

The semi-circular geometry causes wave refraction, and the refracted waves converge on the top of the slope. The shoaling and wave decomposition processes accompany the refraction, leading to a three-dimensional wave transformation combining different phenomena. The resulting wave field can be seen from the simulated free surface elevations at the last time step shown in Fig. 9(a). A Fast Fourier Transform (FFT) analysis is performed for the time series measured at all 39 wave gages. The resulting amplitudes of the first three wave harmonics in the simulations are compared to those from the experiment, as shown in Fig. 9(b). A monochromatic wave is seen at the wave generation boundary. However, two more harmonics develop during the wave transformations over the semi-circular submerged reef. The amplitudes of all harmonics show a general increase over the slope, thanks to the shoaling process. The numerical model captures all three harmonics and shows an agreement in magnitude and trend with the physical experiment.

3.4. Wave breaking over a mild slope

Depth-induced breaking waves are common features in the coastal waters nearshore. The stability of the Godunov-type shock-capturing scheme and the model's ability to represent breaking waves are tested against the experiment on plunging breaking waves over a mild slope presented by Ting and Kirby (1994, 1995). The model's single-phase approach cannot represent the jet formation of the breaking waves. Hence, the breaking wave onset location and energy dissipation due to breaking are considered as criteria in this test. A relaxation zone of 9.5 m is arranged at the left-hand side of the NWT to generate the 5th-order cnoidal wave with a wave height of 0.128 m and period of 5.0 s. The wave propagation zone after the wave generation is 32 m long. The water depth at the wave generation zone is 0.4 m. The mild slope is located 5.8 m downstream from the end of the wave generation zone and rises up to 0.748 m following a 1:35 slope. Four wave gages are arranged at $x = 11.8, 12.8, 13.8$ and 14.1 m from the end of the wave generation zone. The numerical wave tank setup is shown in Fig. 10. 5 vertical cells with a stretching factor of 2.5 are used together with a horizontal cell size of 0.05 m and a CFL criterion of 0.5. The simulation time is 40 s, which is accomplished in 41.6 s using the 12-performance-core M4 Max on a MacBook Pro. The simulated surface elevation time series at the wave gages are compared to the experimental measurements in Fig. 12. The wave breaking event identified at $t = 20$ s in the simulation is illustrated in Fig. 11

The simulated free surface elevation time series exhibit good agreement with experimental measurements at all four wave gauges, as reflected by the relatively low RMSE values. At the first gauge, the incident nonlinear cnoidal wave is well reproduced. An increase in wave crest amplitude is observed at gauge 2, indicating the wave shoaling process. Beyond this point, a significant reduction in crest height occurs after gauge 3, illustrating energy dissipation associated with wave breaking. These observations suggest that the wave breaking onset takes place between gauges 2 and 3. The numerical simulation captures both the location of wave breaking and the associated energy loss with good accuracy, consistent with the experimental results. Following the methodology in previous numerical investigations (Tonelli and Petti, 2010; Derakhti et al., 2016a; Alagan Chella et al., 2016; Iravani et al., 2020; Derakhti et al., 2016b), the cross-shore distribution of the wave height is compared to the measurements presented by Derakhti et al.

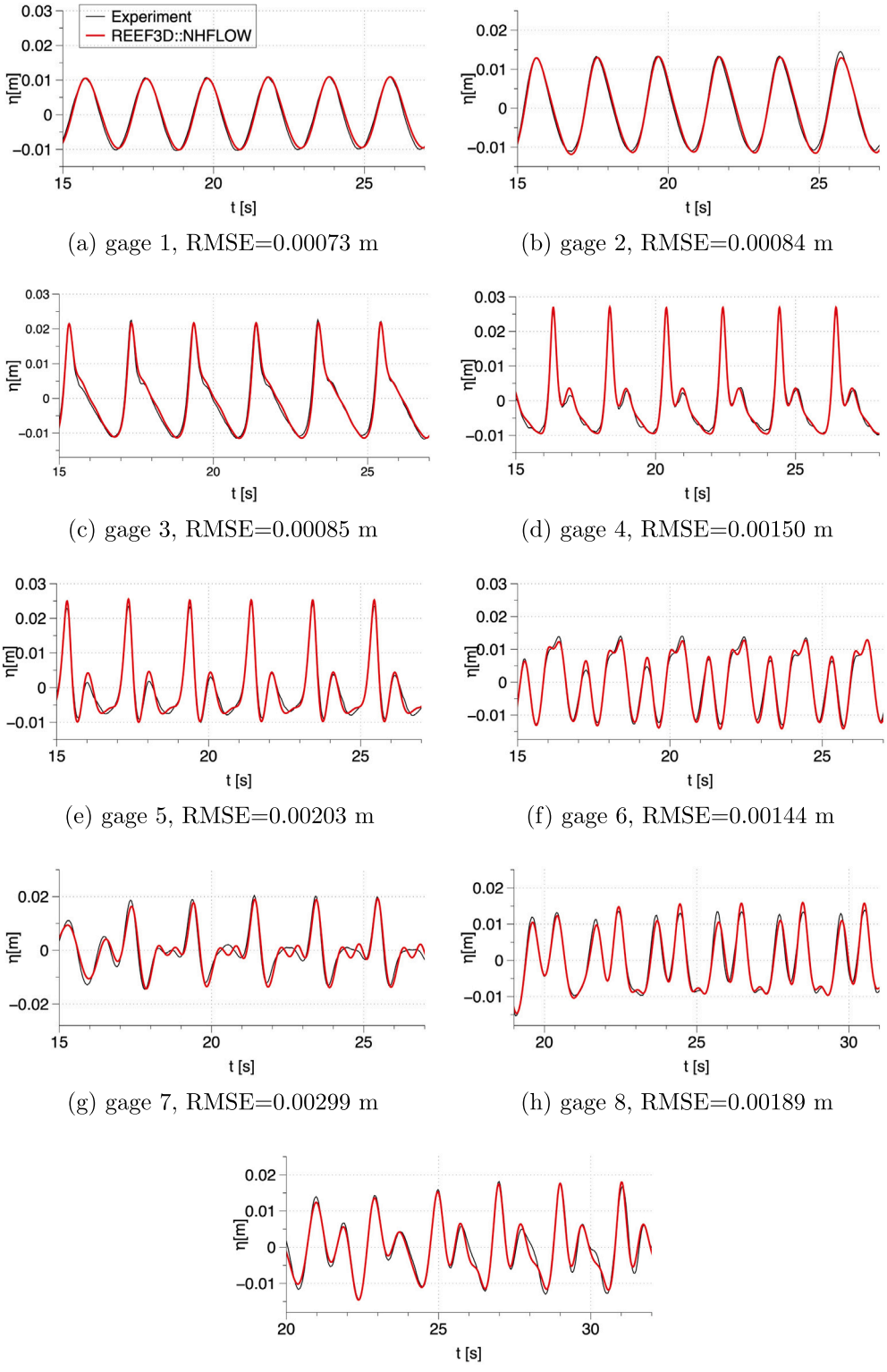

(a) gage 1, RMSE=0.00073 m

(b) gage 2, RMSE=0.00084 m

(c) gage 3, RMSE=0.00085 m

(d) gage 4, RMSE=0.00150 m

(e) gage 5, RMSE=0.00203 m

(f) gage 6, RMSE=0.00144 m

(g) gage 7, RMSE=0.00299 m

(h) gage 8, RMSE=0.00189 m

(i) gage 9, RMSE=0.00215 m

Fig. 4. The surface elevations of the wave transformation over the submerged bar using REEF3D::NHFLOW with 1200 cells in the x-direction and 3 non-uniform vertical layers.

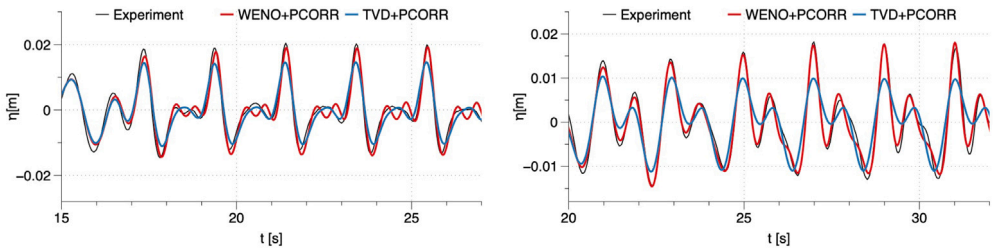

Fig. 5. Comparison of the 5th-order WENO and 2nd-order TVD with van Leer limiter flux reconstruction for the submerged bar using REEF3D::NHFLOW with 1200 cells in the x-direction and 3 non-uniform vertical layers. Both simulations are performed with the pressure correction method (PCORR).

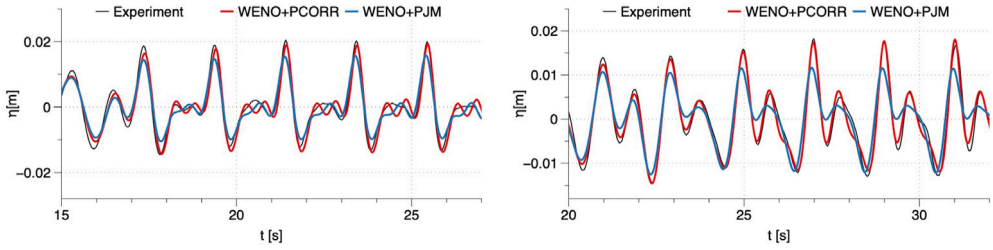

Fig. 6. Comparison of the pressure correction method (PCORR) and the projection method (PJM) for the submerged bar using REEF3D::NHFLOW with 1200 cells in the x-direction and 3 non-uniform vertical layers. Both simulations are performed with the 5th-order WENO flux reconstruction.

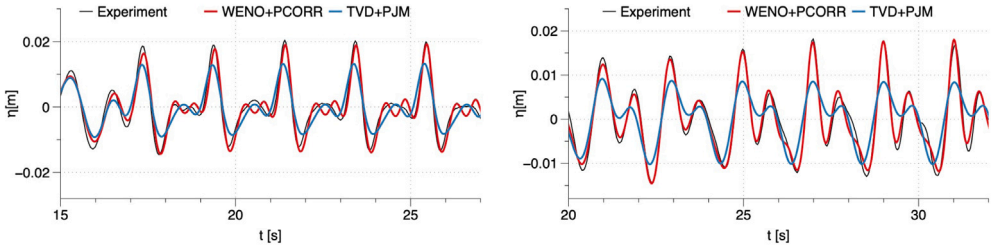

Fig. 7. Comparison of the pressure correction method (PCORR) and the projection method (PJM) for the submerged bar using REEF3D::NHFLOW with 1200 cells in the x-direction and 3 non-uniform vertical layers.

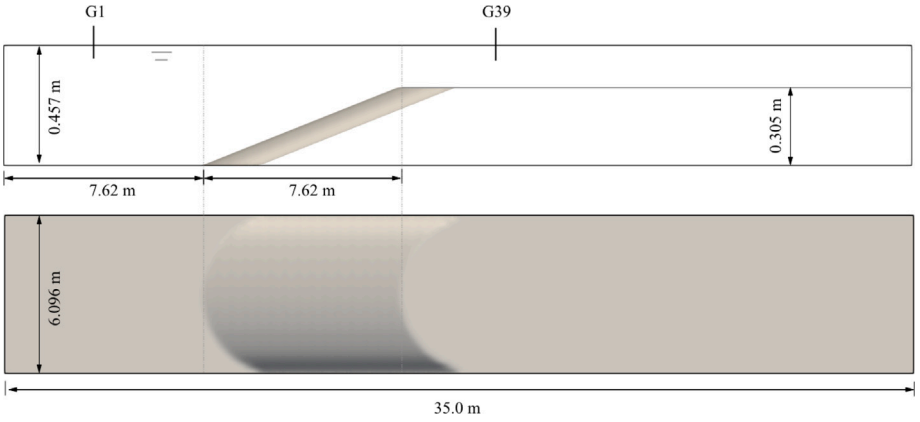

Fig. 8. Numerical wave tank setup in REEF3D::NHFLOW following the experiment from Whalin (1971). The upper figure shows the side view, and the lower figure shows the top view.

Table 1
Wave gauge locations along the longitudinal center line of the numerical wave tank for wave shoaling and refraction over s semi-circular submerged reef.

Gage	x-coord. (m)	Gage	x-coord. (m)	Gage	x-coord. (m)	Gage	x-coord. (m)
1	3.505	11	8.075	21	14.325	31	18.895
2	3.962	12	8.532	22	14.782	32	19.352
3	4.419	13	8.989	23	15.239	33	19.809
4	4.876	14	9.446	24	15.696	34	20.266
5	5.333	15	9.903	25	16.153	35	20.723
6	5.790	16	10.360	26	16.610	36	21.180
7	6.247	17	10.817	27	17.067	37	21.637
8	6.704	18	11.274	28	17.524	38	22.094
9	7.161	19	11.731	29	17.981	39	22.551
10	7.618	20	13.868	30	18.438		

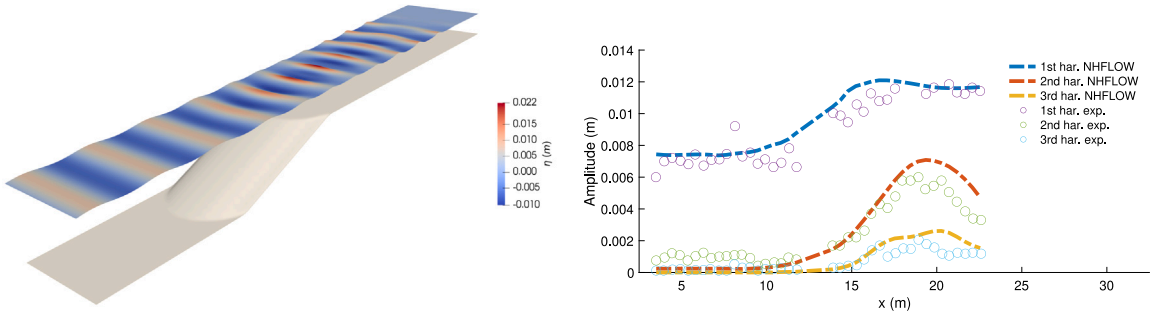

(a) Free surface elevation at the last time step t = 100 s.

(b) Amplitudes of different wave harmonics

Fig. 9. The free surface elevation represented in the numerical simulation and the comparison of the amplitudes of the three harmonics after the wave transformations over a 3D shoal between the numerical simulation and the physical experiment. The RMSE for the 1st, 2nd and 3rd harmonics are 0.00087, 0.00097 and 0.00054 m.

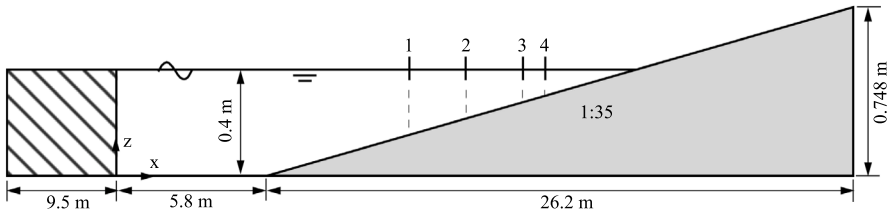

Fig. 10. Numerical wave tank setup for plunging breaking wave over a mild slope in REEF3D::NHFLOW following the experiment from Ting and Kirby (1994, 1995).

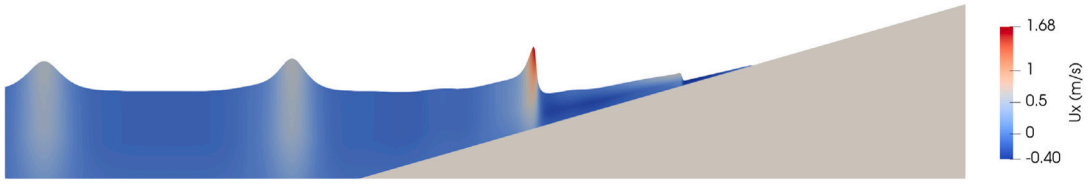

Fig. 11. Wave breaking at$t$ = 20 s in the numerical simulation for wave breaking over a mild slope. The simulation result is scaled by a factor of 10 in the vertical direction for better visualization.

(2016b), as shown in Fig. 13. The simulated cross-shore wave heights match the measurements well overall, although the simulation slightly overestimates the wave height and predicts breaking onset a bit more upstream.

3.5. Wave breaking and run-up

Surf zone and swash zone dynamics are important aspects of coastal engineering. In this section, the numerical model is validated for both wave breaking and run-up on a slope following the experiment presented by Synolakis (1987) and the numerical configurations reported by Ma et al. (2012). In the validation test, the 2D numerical wave tank is 11 m in length along the x-axis. The constant still water depth near the wave generation boundary is d = 0.21 m. A slope is positioned towards the end of the numerical wave tank starting from x = 4 m with a steepness of 1/20. The schematics of the configuration are shown in Fig. 14. A solitary wave is generated at the inlet boundary which has a wave height of 0.0588 m, corresponding to a wave height-to-depth ratio of 0.28. 550 cells along the x-direction (dx = 0.02 m) and 5 uniform σ cells in the vertical direction are used, together with CFL=0.5. The wetting-drying criterion is set to be 2 mm. Turbulence and bottom friction are not included in the simulations. The simulated free surface elevation profile along the x-direction is plotted together with the experimental data, as shown in Fig. 15. In these plots, the free surface elevation is normalized by the still water depth d, the x-coordinate origin is placed at the intersection between the still water level and the slope and the time scale is normalized with $\sqrt{g/d}$. The solitary wave propagates to the slope and shoal before $t\sqrt{g/d}$ = 20 as the

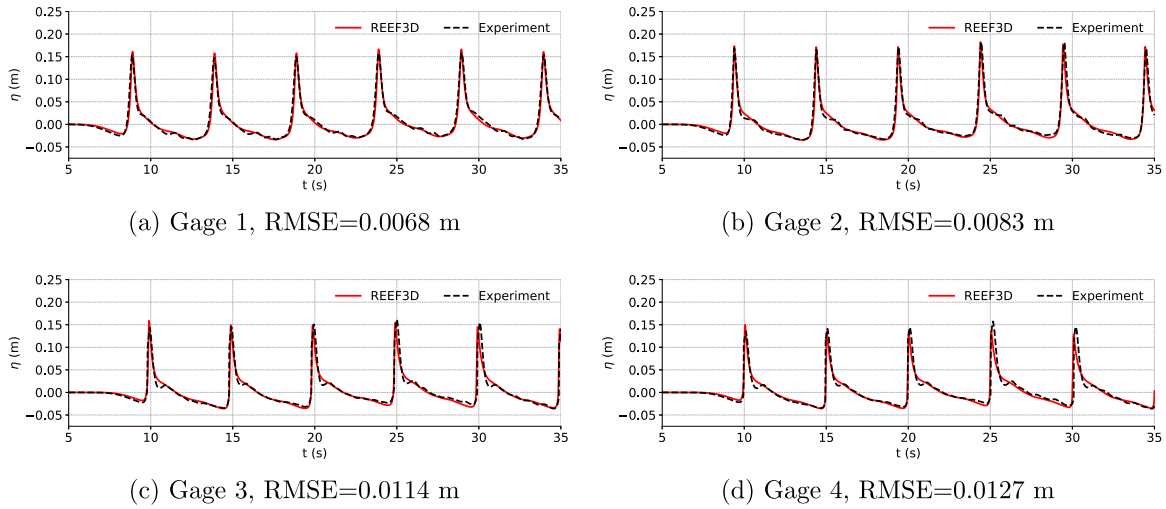

(a) Gage 1, RMSE=0.0068 m (b) Gage 2, RMSE=0.0083 m

(c) Gage 3, RMSE=0.0114 m (d) Gage 4, RMSE=0.0127 m

Fig. 12. The free surface elevation of the plunging breaking wave over a mild slope represented in REEF3D::NHFLOW in comparison to the experimental measurements.

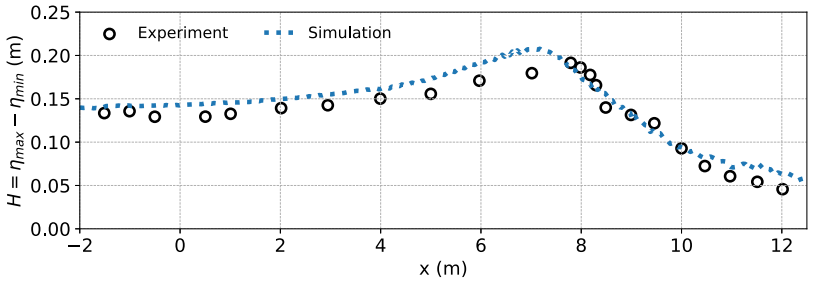

Fig. 13. Cross-shore distribution of the wave height for the plunging breaking case (Ting and Kirby, 1994; Derakhti et al., 2016b).

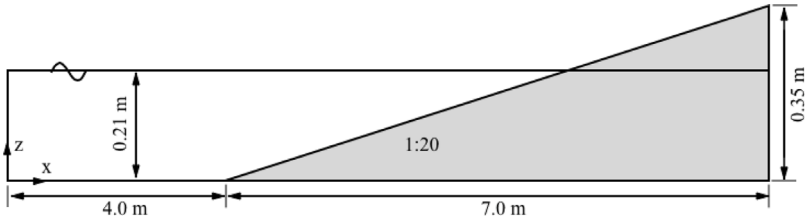

Fig. 14. Numerical wave tank setup in REEF3D::NHFLOW following the configurations by Ma et al. (2012) adapted from the experiment by Synolakis (1987).

wave height increases and the wavefront steepens. Wave breaking takes place around $t\sqrt{g/d} = 20$ and the wave height reduces significantly afterwards. The remaining post-breaking waves run up the slope above the still water level until reaching the maximum run-up and a rundown process starts around $t\sqrt{g/d} = 50$. The wave surface elevation and the horizontal particle velocity components in the numerical wave tank are also visualized in Fig. 16. The wave shoaling, breaking, run-up and run-down processes are all represented by the numerical simulation with a favorable agreement with the experiment. The wave-breaking time, location and post-breaking energy dissipation, as well as the wave front locations in the swash zone, show a good visual agreement between the simulations and the experiment. The maximum run-up from the simulation is 0.3251 m at $x = 10.46$ m, which is only 1.92% lower than the theoretical maximum run-up using the formula proposed by Synolakis (1987). The good prediction of the maximum run-up also shows a correct representation of the breaking wave energy dissipation and confirms the effectiveness of the wetting-drying algorithms. The shock-capturing nature of the new wave model is able to capture the initiation of wave breaking and represent the energy dissipation even without turbulence models in this scenario.

4. Real-world applications

4.1. Mehamn harbor

Mehamn is located in northern Norway and is the northernmost harbor that the Norwegian ferry line Hurtigruten operates. The harbor has an opening to the north and is surrounded by two peninsulas to the west and east. Historically, the small boats moored at the inner harbor marina have experienced large waves under certain sea states, despite the relatively sheltered location. This led to an experimental investigation into the wave propagation characteristics in the harbor (Vold and Lothe, 2009), especially the strong diffraction around the peninsulas. The proposed wave model aims to reproduce the experimental investigations and validate the model's capability of representing complex nonlinear wave transformations over natural bathymetry and irregular coastlines. The satellite image of the investigation site and the experimental configuration are shown in Fig. 17.

The experiment is performed at a scale of 1:80, representing a full-scale domain of 1.76 km long and 1.44 km wide with the deepest water depth of 40 m. A 9.5 m long wavemaker is located at the northern boundary to generate uni-directional irregular waves. A solid structure

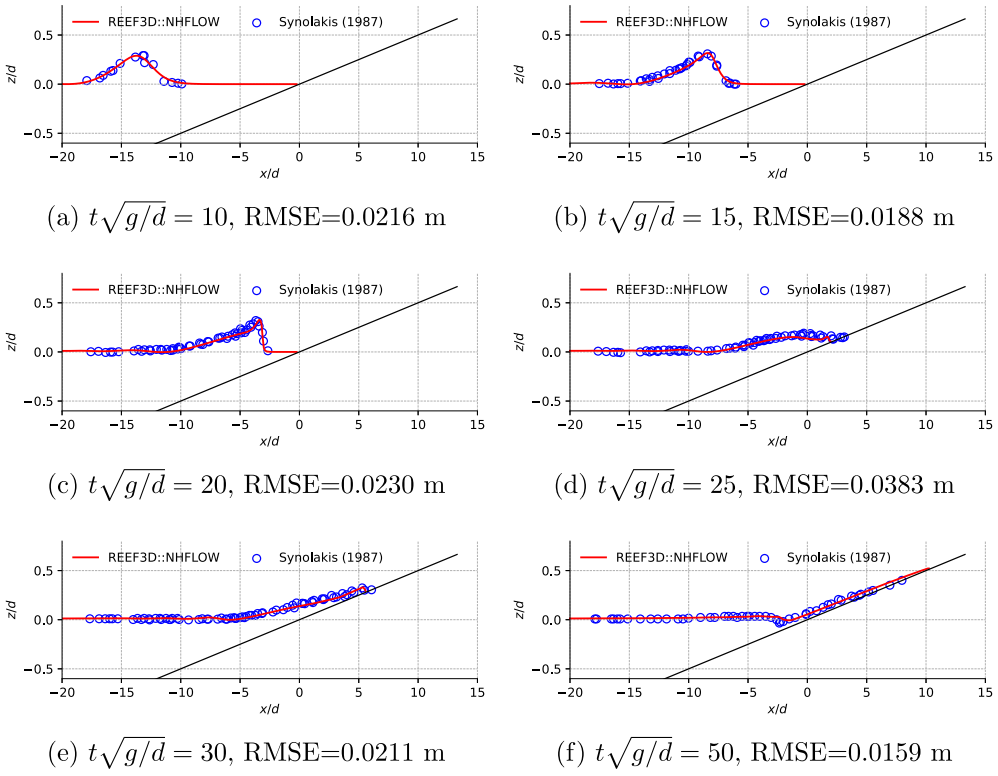

Fig. 15. The surface elevations of the wave breaking and run-up over a plane beach.

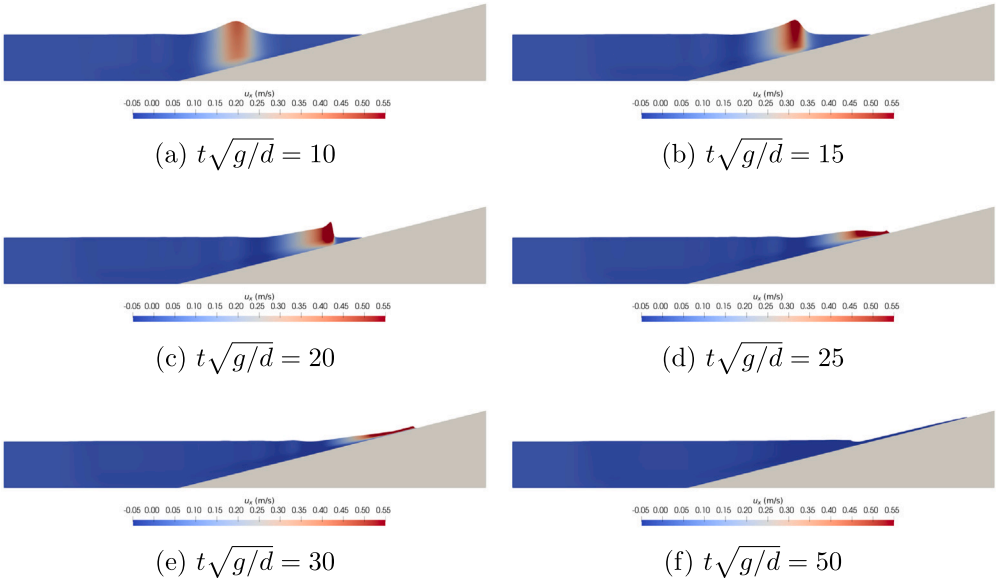

Fig. 16. The surface elevations and horizontal particle velocities visualized for the wave breaking and run-up over a plane beach. A scale factor of 5 is applied in the vertical direction for the purpose of visualization.

is placed to cover the rest of the northern boundary due to the limited dimensions of the wavemaker. A wave absorption area is located on the southern boundary. Nine wave gages are arranged along the coastline of the harbor. The wave gage 1 is used to calibrate the incoming waves and gage 9 represents the small boat marina. The numerical simulation follows the same configuration but is performed at full scale. Two irregular wave scenarios are investigated, one has a significant wave height H_s = 3.5 m and a peak period T_p = 12 s, and another with H_s = 4.5 m and T_p = 15 s. A 2D convergence study shows a horizontal cell size of 4 m is sufficient to represent the input JONSWAP wave spectrum formulated by DNV (DNV-GL, 2011). The time steps are constrained with a CFL number of 0.5.

Five vertical σ cells are used together with a stretching factor $\alpha = 2.5$ to capture the high-frequency dispersive waves in the irregular wave field. Each simulation is performed for 3.56 h, and the free surface elevation time series of the last 3 h are used for the FFT analysis. The

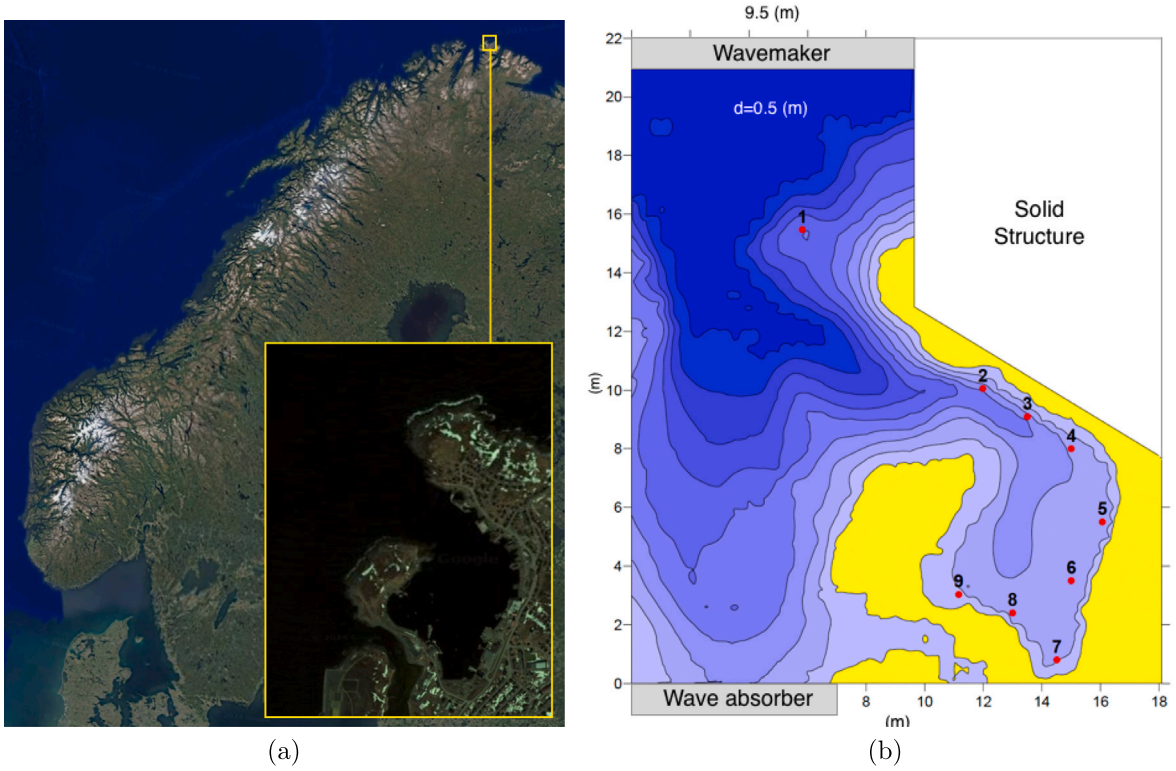

Fig. 17. (a) Location and satellite image of Mehamn harbor from 2012. (b) Physical experiment configuration of the Mehamn harbor (dimensions in experimental scale with a scale factor 1:80).

simulations take 6.39 h using two AMD EPYC 7763 64-Core processors, achieving an elapsed computational time to simulation time ratio of 1.8.

The simulated free surface elevations of the two scenarios are shown in Fig. 18. The incident irregular waves encounter the eastern peninsula first. Here, the water depth variation and the coastline geometry lead to the change of the principal wave direction towards the inner harbor. A small proportion of the waves are also reflected in a radiating pattern. The waves continue towards the inner harbor until interacting with the western peninsula, where the local bathymetry and coastline conditions change the principal direction westwards to the small boat marina near the wave gage 9. A strong wave diffraction pattern is observed at the harbor entry between the two peninsulas. This series of wave transformations is the reason for the high waves inside the harbor despite the fact that the harbor is sheltered by two peninsulas.

The significant wave heights at the wave gages from the numerical simulations are compared to the experimental measurements in Fig. 19. In both scenarios, the significant wave heights decrease along the coast towards the inner harbor and marina, following the number sequence of the wave gages, though slight increases in the wave heights are seen near gage 6. Despite the general trend of decreasing wave heights, wave gage 9 still measures a significant wave height of about 0.3 m in both cases. The numerically calculated H_s agree with the experiment both in terms of magnitude and the general trend. This indicates a plausible representation of the complex and combined wave transformations of shoaling, refraction, reflection and diffraction.

4.2. Ericeira and computational performance

The new wave model is fully parallelized with MPI and thus enables large-scale simulations with multi-core computational infrastructures. In this section, the wave propagation simulation at Ericeira is used to demonstrate the model's computational efficiency and scalability. Ericeira is located on the west coast of Portugal and is the first European site among World Surfing Reserves and features many surfing beaches with different breaking wave characteristics.

The breaking wave types at each beach was numerically identified using the fully-nonlinear potential flow model within the REEF3D framework (Gomes et al., 2024). The satellite image of the Ericeira coast is shown in Fig. 20, where three of the 16 beaches are highlighted. This coastal area has varying bathymetry, irregular coastline, breakwaters, and different breaking waves and serves as an ideal test case where the different functionalities of the proposed model are activated and engaged. The domain of 8.68 km × 18.42 km is discretized into slightly over 50 million cells, with 4.0 m horizontal cells and 5 vertical cells in all simulations. A CFL number of 0.75 is used. These simulations are performed on the supercomputer Betzy, which is a part of the Norwegian national e-infrastructure provided by Sigma2. The supercomputer has 1338 computational nodes; each node has 128 CPU cores with the CPU type of AMD Epyc 7742 (2.25 GHz). It has a total memory of 344 TB with 256 GB per node. The supercomputer runs with the Red Hat Enterprise Linux 7 operating system.

Fig. 20 shows the simulated large-scale wave surface elevations along the Ericeira coast in the middle panel. Close-up views of the wave fields are presented in the right panel of Fig. 20 for the three highlighted beaches, where the wave shoaling, refraction and diffraction around the breakwater are resolved in details. 100 iterations are simulated and the elapsed time are compared in the form of a speed-up factor defined as the elapsed time with a single core divided by the elapsed time with multiple cores. Fig. 21(a) shows the speed-up factor of the simulation using different numbers of computational cores in comparison to a serial simulation with a single core. The corresponding numbers of cells per core are also indicated in the secondary x-axis in the figure. It is seen that the model's computational speed increases nearly linearly with the increasing number of computational cores across the tested range up to 2560 cores. The supercomputer Betzy is

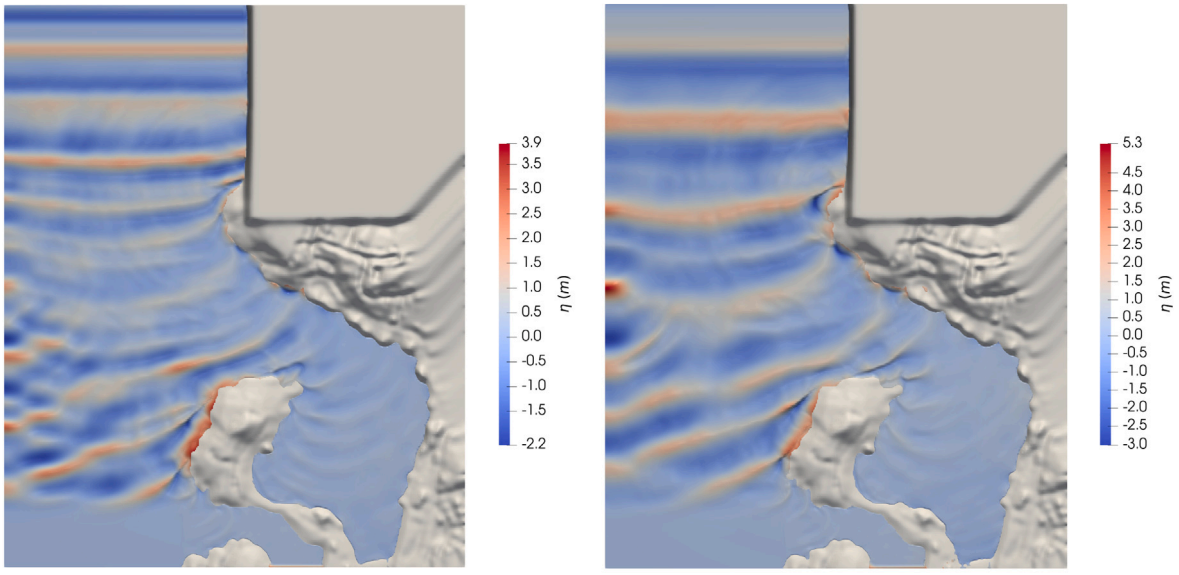

(a) $H_s = 3.5$ m, $T_p = 12$ s (b) $H_s = 4.5$ m, $T_p = 15$ s

Fig. 18. The free surface elevations at the last time step in the simulations of uni-directional irregular wave propagation into Mehamn harbor with REEF3D::NHFLOW.

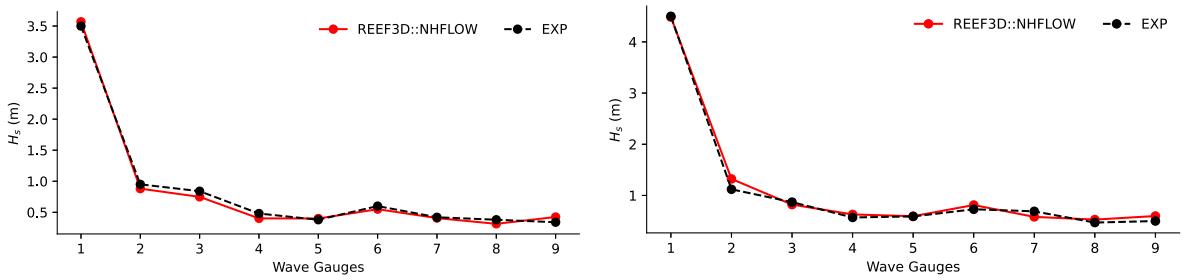

(a) $H_s = 3.5$ m, $T_p = 12$ s (b) $H_s = 4.5$ m, $T_p = 15$ s

Fig. 19. Comparison between the simulated and experimental H_s for uni-directional irregular wave propagation into Mehamn harbor using REEF3D::NHFLOW.

optimized for large simulations with minimum of 4 nodes (512 cores), which is reflected in the fact that the computational speedup increase is slightly more than linear when using more than 512 cores.

Another series of tests is performed with the same number of 512 computational cores but different vertical cell counts. Fig. 21(b) shows the ratio of computational time with multiple vertical cells divided by the computational time with a single vertical cell T/T_0 while using the same horizontal cell size. The computational time increases almost linearly with the vertical cell numbers, despite that a slightly greater increase in computational time is observed when increasing from 2 to 3 vertical cells. These tests show the model's good potential for large-scale and computationally demanding simulations using multiple processors. Furthermore, the computational efficiency of the model is not limited by the number of vertical cells.

5. Conclusions

The new non-hydrostatic flow and wave model REEF3D::NHFLOW is presented in the current paper. The model is designed with a unique combination of the σ-coordinate grid, a Godunov-type scheme with shock-capturing properties, WENO flux reconstruction, non-hydrostatic pressure correction and deferred correction for sigma terms in the Poisson equation. Through this novel implementation, the model can represent coastal wave transformations in an efficient and accurate manner. With 5 vertical cells, the model represents linear wave dispersion relation over a wide range of water depth up to $kd = 80$. The 2D and 3D wave transformations over a submerged bar and a semi-circular submerged reef show an accurate representation of wave shoaling, refraction and decomposition. Wave breaking and run-up over slopes are also well-represented thanks to the model's inherent shock-capturing nature and the effective wetting-drying algorithm. The agreement between the simulated H_s and the experimental measures for wave propagation into Mehamn harbor demonstrates the model's capability for modeling real-world complex wave fields with combined shoaling, refraction, reflection and diffraction over varying natural bathymetry. In addition, the model is fully parallelized based on the domain decomposition strategy and can thus be employed for large-scale wave propagation problems with high performance. The simulation of the Ericeira coastline has shown near-linear scalability with the increasing number of processors and near-linear computational time increase with the increased number of vertical cells. As an outlook for future research, the model will be further feature-enhanced to address e.g. fluid–structure interaction, wind and current effects and sediment transport. While the model reliably captures breaking waves in the presented cases, it does not fully represent the details of turbulence effects and vorticity generation. The incorporation of breaking wave models and turbulence models will help improve the representation of the breaking wave physics for a broader range of scenarios. This will be explored and included in future development.

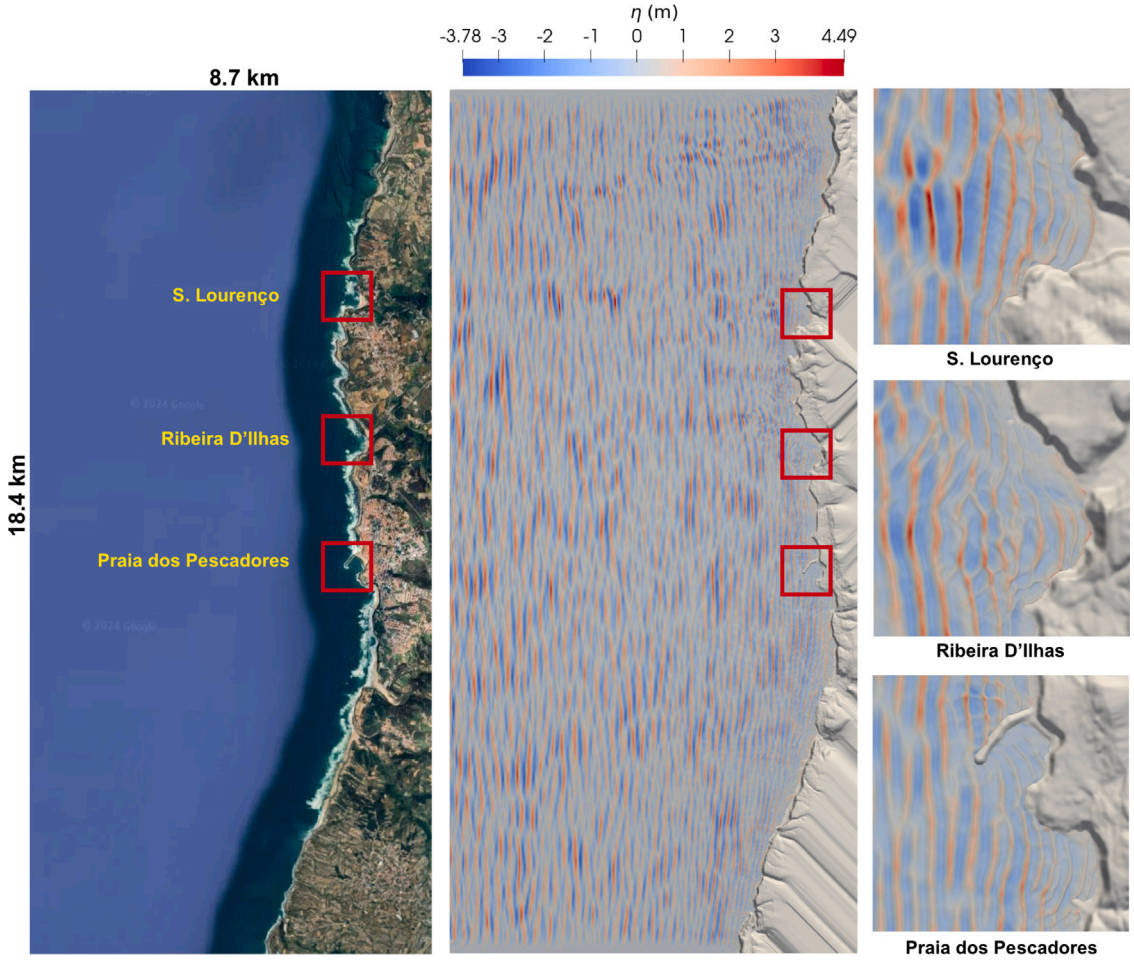

Fig. 20. Left panel: Google Earth satellite view of the surfing beaches along the Ericeira coast; Center panel: Surface elevation from the numerical simulation with $dx = 4$ m for the domain of 8.68 km × 18.42 km size; Right panel: zoomed-in view of simulated surface elevations at three selected beaches.

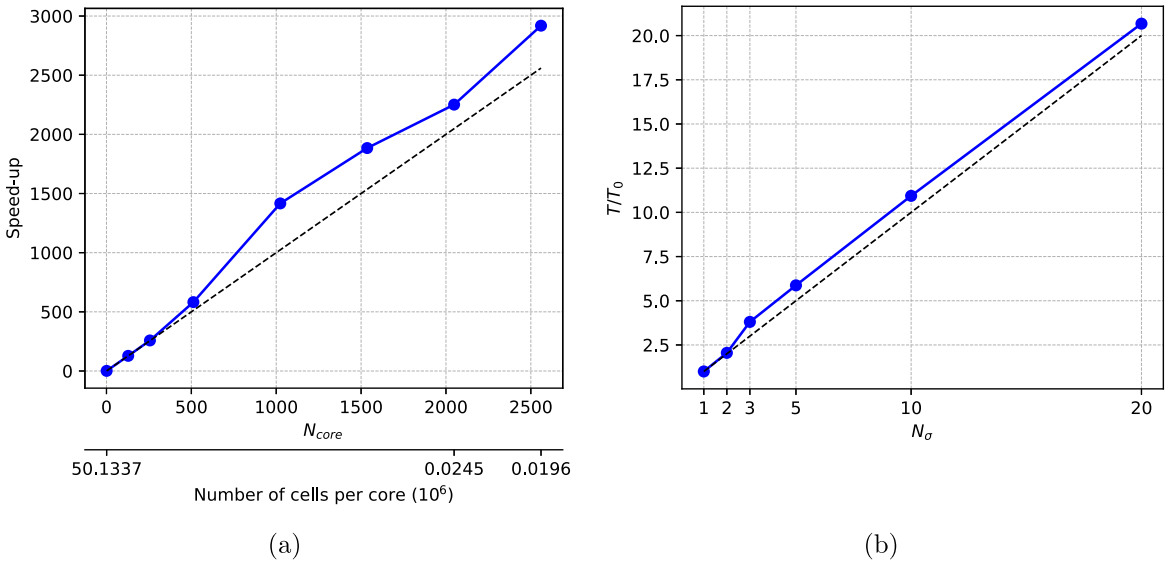

Fig. 21. The numerical scalability with parallel computing on UNINETT Sigma2's Betzy HPC infrastructure and simulation time sensitivity to the vertical resolution. (a) The computational speedup with an increasing number of computer cores for the Ericeira case with 50 million cells. (b) Computational time increase T/T_0 with increasing vertical σ grid resolution.

Table 2
Relative phase-velocity in the linear dispersion test in Section 3.1, comparing different vertical grid configurations.

kd	Nz=1 uniform	Nz=2 uniform	Nz=3 uniform	Nz=5 uniform	Nz=5 α = 1.5	Nz=5 α=2.5	Nz=5 α=3.5
0.3	1.0075	1.0067	1.0059	1.0052	1.0054	1.0058	1.0062
0.4	1.0086	1.0041	1.0028	1.0019	1.0021	1.0025	1.0031
0.5	1.0119	1.0040	1.0029	1.0023	1.0023	1.0027	1.0032
0.6	1.0152	1.0051	1.0031	1.0017	1.0021	1.0028	1.0037
0.7	1.0190	1.0057	1.0033	1.0020	1.0023	1.0029	1.0039
0.8	1.0238	1.0069	1.0038	1.0021	1.0024	1.0033	1.0047
0.9	1.0279	1.0079	1.0041	1.0021	1.0025	1.0035	1.0052
1.0	1.0323	1.0093	1.0050	1.0027	1.0032	1.0043	1.0062
2.0	1.0392	1.0131	1.0071	1.0034	1.0041	1.0060	1.0092
3.0	0.8967	1.0078	1.0064	1.0045	1.0049	1.0056	1.0067
4.0		1.0048	1.0044	1.0039	1.0040	1.0046	1.0047
5.0		1.0031	1.0042	1.0039	1.0039	1.0038	1.0035
6.0		1.0000	1.0043	1.0039	1.0039	1.0037	1.0035
7.0		0.9956	1.0048	1.0040	1.0039	1.0037	1.0036
8.0		0.9769	1.0035	1.0039	1.0039	1.0038	1.0037
9.0		0.9507	1.0030	1.0041	1.0040	1.0039	1.0037
10.0		0.9168	1.0027	1.0039	1.0039	1.0038	1.0037
20.0		0.6768	0.9444	1.0054	1.0050	1.0041	1.0038
30.0			0.7473	1.0021	1.0034	1.0043	1.0038
40.0			0.5995	0.9908	0.9954	1.0012	1.0041
50.0				0.9635	0.9766	0.9970	1.0030
60.0				0.9132	0.9367	0.9858	1.0020
70.0				0.8458	0.8793	0.9571	0.9998
80.0				0.7595	0.8007	0.9199	0.9941
90.0				0.7027	0.7317	0.8713	0.9855
100.0				0.6075	0.6569	0.8104	0.9689

CRediT authorship contribution statement

Hans Bihs: Writing – review & editing, Writing – original draft, Visualization, Validation, Software, Project administration, Methodology, Investigation, Formal analysis, Conceptualization. **Widar Weizhi Wang:** Writing – review & editing, Writing – original draft, Visualization, Validation, Methodology, Formal analysis, Conceptualization.

Declaration of competing interest

The authors declare that they have no known competing financial interests or personal relationships that could have appeared to influence the work reported in this paper.

Acknowledgments

The authors thank the funding by the European Union (ERC, PARTRES, 101045646). Views and opinions expressed are however those of the authors only and do not necessarily reflect those of the European Union or the European Research Council Executive Agency. Neither the European Union nor the granting authority can be held responsible for them. We are also grateful for the bathymetry data for Ericeira provided by Tiago Gomes under the EEA Norway-Portugal project FBR_OC2_47 'Coastal Wave Modelling in the World Surfing Reserve of Ericeira'. A few of the simulations in Section 4 were performed on the supercomputer Betzy provided by UNINETT Sigma2 — the National Infrastructure for High-Performance Computing and Data Storage in Norway.

Appendix

See Tables 2 and 3.

Data availability

Data will be made available on request.

Table 3
Relative phase-velocity in the linear dispersion test in Section 3.1, comparing different numerical schemes: WENO-PCORR, WENO-PJM and TVD-PCORR. 5 vertical cells and a stretching factor of 3.5 are used in all cases.

kd	WENO-PCORR	WENO-PJM	TVD-PCORR
0.3	1.0062	1.0060	1.0036
0.4	1.0031	1.0032	1.0031
0.5	1.0032	1.0031	1.0026
0.6	1.0037	1.0035	1.0028
0.7	1.0039	1.0040	1.0033
0.8	1.0047	1.0047	1.0040
0.9	1.0052	1.0054	1.0053
1.0	1.0062	1.0062	1.0052
2.0	1.0092	1.0104	1.0074
3.0	1.0067	1.0086	1.0028
4.0	1.0047	1.0067	0.9994
5.0	1.0035	1.0056	0.9978
6.0	1.0035	1.0054	0.9971
7.0	1.0036	1.0050	0.9965
8.0	1.0037	1.0071	0.9961
9.0	1.0037	1.0066	0.9955
10.0	1.0037	1.0091	0.9952
20.0	1.0038	1.0117	0.9906
30.0	1.0038	1.0176	0.9874
40.0	1.0041	1.0244	0.9865
50.0	1.0030	1.0327	0.9840
60.0	1.0020	1.0367	0.9800
70.0	0.9998	1.0560	0.9758
80.0	0.9941	1.0718	0.9675
90.0	0.9855	1.0816	0.9603
100.0	0.9689	1.1018	0.9470

References

Afshar, M.A., Bingham, H.B., 2017. Solving the linearized forward-speed radiation problem using a high-order finite difference method on overlapping grids. Appl. Ocean Res. 69, 220–244.

Aggarwal, A., Bihs, S., Myrhaug, D., 2019. Estimation of breaking wave properties and their interaction with a jacket structure. J. Fluids Struct. 91 (102722).

Alagan Chella, M., Bihs, H., Myrhaug, D., Muskulus, M., 2016. Hydrodynamic characteristics and geometric properties of plunging and spilling breakers over impermeable slopes. Ocean. Model. (ISSN: 1463-5003) 103, 53–72. http://dx.doi.org/10.1016/j.ocemod.2015.11.011, Waves and coastal, regional and global processes.

Ashby, S.F., Falgout, R.D., 1996. A parallel mulitgrid preconditioned conjugate gradient algorithm for groundwater flow simulations. Nucl. Sci. Eng. 124 (1), 145–159.
Beji, S., Battjes, J.A., 1993. Experimental investigation of wave propagation over a bar. Coast. Eng. 19, 151–162.
Bihs, H., Kamath, A., Alagan Chella, M., Aggarwal, A., Arntsen, Ø.A., 2016. A new level set numerical wave tank with improved density interpolation for complex wave hydrodynamics. Comput. & Fluids 140, 191–208.
Bihs, H., Kamath, A., Alagan Chella, M., Arntsen, Ø.A., 2019. Extreme wave generation, breaking, and impact simulations using wave packets in REEF3D. J. Offshore Mech. Arct. Eng. 141 (041802–1).
Bingham, H.B., Zhang, H., 2007. On the accuracy of finite-difference solutions for nonlinear water waves. J. Engrg. Math. 58, 211–228.
Casulli, V., Stelling, G.S., 1998. Numerical simulation of 3D quasi-hydrostatic, free-surface flows. J. Hydraul. Eng. 124 (7), 678–686.
Chen, Q., Kelly, D.M., Zang, J., 2019. On the relaxation approach for wave absorption in numerical wave tanks. Ocean Eng. (ISSN: 0029-8018) 187, 106210.
Chorin, A., 1968. Numerical solution of the Navier-Stokes equations. Math. Comp. 22, 745–762.
Derakhti, M., Kirby, J.T., Shi, F., Ma, G., 2016a. NHWAVE: Consistent boundary conditions and turbulence modeling. Ocean. Model. (ISSN: 1463-5003) 106, 121–130. http://dx.doi.org/10.1016/j.ocemod.2016.09.002.
Derakhti, M., Kirby, J.T., Shi, F., Ma, G., 2016b. Wave breaking in the surf zone and deep-water in a non-hydrostatic RANS model. Part 1: Organized wave motions. Ocean. Model. (ISSN: 1463-5003) 107, 125–138. http://dx.doi.org/10.1016/j.ocemod.2016.09.001.
DNV-GL, 2011. Modelling and analysis of marine operations. In: DNV-RP-H103. Det Norske Veritas - Germanischer Lloyd, Veritasveien 1, Høvik, Norway.
Ducrozet, G., Bingham, H.B., Engsig-Karup, A.P., Ferrant, P., 2010. High-order finite difference solution for 3D nonlinear wave-structure interaction. In: 9 th International Conference on Hydrodynamics October 11-15. 2010 Shanghai, China.
Ducrozet, G., Bonnefoy, F., Le Touzé, D., Ferrant, P., 2012. A modified high-order spectral method for wavemaker modeling in a numerical wave tank. Eur. J. Mech. B Fluids 34, 19–34.
Engsig-Karup, A., Bingham, H., Lindberg, O., 2009. An efficient flexible-order model for 3D nonlinear water waves. J. Comput. Phys. (ISSN: 0021-9991) 228 (6), 2100–2118.
Engsig-Karup, A.P., Madsen, M.G., Glimberg, S.L., 2012. A massively parallel GPU-accelerated model for analysis of fully nonlinear free surface waves. Internat. J. Numer. Methods Fluids 70, 20–36.
Fuhrman, D.R., Bingham, H.B., 2004. Numerical solutions of fully non-linear and highly dispersive Boussinesq equations in two horizontal dimensions. Internat. J. Numer. Methods Fluids 44, 231–255.
Gomes, T., Bihs, H., Wang, W., Vaz, G., 2024. Simulating waves at the beaches of the ericeira world surfing reserve. In: Proceedings of the ASME 2024 43rd International Conference on Ocean, Offshore and Arctic Engineering OMAE2024 Singapore.
Gottlieb, S., Shu, C.W., 1998. Total variation diminishing Runge-Kutta schemes. Math. Comp. 67 (221), 73–85.
Grilli, S.T., Guyenne, P., Dias, F., 2001. A fully non-linear model for three-dimensional overturning waves over an arbitrary bottom. Internat. J. Numer. Methods Fluids 35, 829–867.
Grilli, S.T., Skourup, J., Svendsen, I.A., 1989. An efficient boundary element method for nonlinear water waves. Eng. Anal. Bound. Elem. 6 (2), 97–107.
Harten, A., Lax, P., van Leer, B., 1983. On upstream differencing and godunov-type schemes for hyperbolic conservation laws.. SIAM Rev. 25 (1).
Higuera, P., Lara, L.J., Losada, I.J., 2013. Realistic wave generation and active wave absorption for Navier-Stokes models application to OpenFOAM. Coast. Eng. 71, 102–118.
Iravani, N., Badiei, P., Brocchini, M., 2020. Novel free surface boundary conditions for spilling breaking waves. Coast. Eng. (ISSN: 0378-3839) 159, 103717. http://dx.doi.org/10.1016/j.coastaleng.2020.103717.
Jacobsen, N.G., Fuhrman, D.R., Fredsøe, J., 2012. A wave generation toolbox for the open-source CFD library: OpenFOAM. Internat. J. Numer. Methods Fluids 70 (9), 1073–1088.
Jeschke, A., Pedersen, G.K., Vater, S., Behrens, J., 2017. Depth-averaged non-hydrostatic extension for shallow water equations with quadratic vertical pressure profile: equivalence to Boussinesq-type equations. Internat. J. Numer. Methods Fluids 84 (10), 569–583.
Jiang, G.S., Shu, C.W., 1996. Efficient implementation of weighted ENO schemes. J. Comput. Phys. 126, 202–228.
Kamath, A., Wang, W., Pakozdi, C., Bihs, H., 2023. Identification and investigation of extreme events using an arbitrary Lagrangian–Eulerian approach with a Laplace equation solver and coupling to a Navier–Stokes solver. J. Offshore Mech. Arct. Eng. 145 (6), 061902.
Larsen, B.E., Fuhrman, D.R., 2018. On the over-production of turbulence beneath surface waves in Reynolds-averaged Navier–Stokes models. J. Fluid Mech. 853, 419–460.
Li, B., 2008. A 3-D model based on Navier–Stokes equations for regular and irregular water wave propagation. Ocean Eng. (ISSN: 0029-8018) 35 (17), 1842–1853.
Li, B., Fleming, C.A., 1997. A three dimensional multigrid model for fully nonlinear water waves. Coast. Eng. 30 (3–4), 235–258.
Liang, Q., Marche, F., 2009. Numerical resolution of well-balanced shallow water equations with complex source terms. Adv. Water Resour. 32, 873–884.
Lin, P., Li, C.W., 2002. A σ-coordinate three-dimensional numerical model for surface wave propagation. Internat. J. Numer. Methods Fluids 38 (11), 1045–1068.
Lynnett, P.J., Wu, T.R., Liu, P.L., 2002. Modeling wave runup with depth-integrated equations. Coast. Eng. 46 (89–107).
Ma, G., Farahani, A.A., Kirby, J.T., Shi, F., 2016. Modeling wave-structure interactions by an immersed boundary method in a σ-coordinate model. Ocean Eng. 125, 238–247.
Ma, G., Kirby, J.T., Shi, F., 2013. Numerical simulation of tsunami waves generated by deformable submarine landslides. Ocean. Model. (ISSN: 1463-5003) 69, 146–165.
Ma, G., Shi, F., Hsiao, S.-C., Wu, Y.-T., 2014. Non-hydrostatic modeling of wave interactions with porous structures. Coast. Eng. 91, 84–98.
Ma, G., Shi, F., Kirby, J.T., 2012. Shock-capturing non-hydrostatic model for fully dispersive surface wave processes. Ocean. Model. 43–43, 22–35.
Madsen, R., 2009. Udvikling af en Skalerbar Parallel LøSer Af Laplaceligningen for Ikke-Lineære VandbøLger. Danmarks Tekniske Universitet, DTU Informatik.
Madsen, P.A., Bingham, H.B., Liu, H., 2002. A new Boussinesq method for fully nonlinear waves from shallow to deep water. J. Fluid Mech. 462, 1–30.
Madsen, P.A., Murray, R., Sørensen, O.R., 1991. A new form of the Boussinesq equations with improved linear dispersion characteristics. Coast. Eng. 15, 371–388.
Nwogu, O., 1993. Alternative form of Boussinesq equations for nearshore wave propagation. J. Waterw. Port Coast. Ocean. Eng. 119 (6), 618–638.
Ohyama, T., Kioka, W., Tada, A., 1995. Applicability of numerical models to nonlinear dispersive waves. Coast. Eng. 24, 297–313.
Pakozdi, C., Kamath, A., Wang, W., Bihs, H., 2022. Application of arbitrary lagrangian–eulerian strips with fully nonlinear wave kinematics for force estimation. Mar. Struct. 83 (103190).
Peregrine, D.H., 1967. Long waves on a beach. J. Fluid Mech. 27 (4), 815–827.
Peric, M., Ferziger, J., 2001. Computational Methods for Fluid Dynamics. Springer.
Roeber, V., Cheung, K.F., 2012. Boussinesq-type model for energetic breaking waves in fringing reef environments. Coast. Eng. (ISSN: 0378-3839) 70, 1–20.
Roeber, V., Cheung, K., Kobayashi, M., 2010. Shock-capturing Boussinesqtype model for nearshore wave processes. Coast. Eng. 57, 407–423.
Roelvink, D., Reniers, A., van Dongeren, A., van Thiel de Vries, J., 2009. Modelling storm impacts on beaches, dunes and barrier islands. Coast. Eng. 56, 1133–1152.
Shi, F., Kirby, J.T., Harris, J.C., Geiman, J.D., Grilli, S.T., 2023. A high-order adaptive time-stepping TVD solver for Boussinesq modeling of breaking waves and coastal inundation. Ocean. Model. 43–44, 36–51.
Smit, P.B., Stelling, G.S., Roelvink, D., van Thiel de Vries, J., McCall, R., van Dongeren, A., Zwinkels, R., Jacobs, R., 2010. XBeach: Non-hydrostatic model: Validation, verification and model description. Tech. Rep. Delft Univ. Technol..
Stelling, G., Zijlema, M., 2003. An accurate and efficient finite-difference algorithm for non-hydrostatic free-surface fow with application to wave propagation. Internat. J. Numer. Methods Fluids 43, 1–23.
Svendsen, I.A., 1974. Cnoidal Waves Over a Gently Sloping Bottom. Tech. Univ. Denmark, Lyngby, ISVA, Ser. Pap. 6..
Synolakis, C.E., 1987. The runup of solitary waves. J. Fluid Mech. 185, 523–545.
Ting, F.C., Kirby, J.T., 1994. Observation of undertow and turbulence in a laboratory surf zone. Coast. Eng. (ISSN: 0378-3839) 24 (1), 51–80. http://dx.doi.org/10.1016/0378-3839(94)90026-4.
Ting, F.C.K., Kirby, J.T., 1995. Dynamics of surf-zone turbulence in a strong plunging breaker. Coast. Eng. 24, 177–204.
Tonelli, M., Petti, M., 2010. Finite volume scheme for the solution of 2D extended Boussinesq equations in the surf zone. Ocean Eng. (ISSN: 0029-8018) 37 (7), 567–582. http://dx.doi.org/10.1016/j.oceaneng.2010.02.004.
Vold, S., Lothe, A.E., 2009. Mehamn - Modellforsøk, Technical Report, SBF IN F09203 SINTEF Byggforsk, Trondheim.
van der Vorst, H., 1992. BiCGStab: A fast and smoothly converging variant of bi-CG for the solution of nonsymmetric linear systems. SIAM J. Sci. Stat. Comput. 13, 631–644.
Wang, W.W., Kamath, A., Pakozdi, C., Bihs, H., 2020a. A comparison of different wave modelling techniques in an open-source hydrodynamic framework. J. Mar. Sci. Eng. 8 (7), 526.
Wang, W.W., Martin, T., Kamath, A., Bihs, H., 2020b. An improved depth-averaged non-hydrostatic shallow water model with quadratic pressure approximation. Internat. J. Numer. Methods Fluids 92 (8), 803–824.
Wang, W., Pakozdi, C., Kamath, A., Bihs, H., 2021. A fully nonlinear potential flow wave modelling procedure for simulations of offshore sea states with various wave breaking scenarios. Appl. Ocean Res. 117 (102898).
Wang, W.W., Pakozdi, C., Kamath, A., Bihs, H., 2022a. A flexible fully nonlinear potential flow model for wave propagation over the complex topography of the Norwegian coast. Appl. Ocean Res. 122 (103103).
Wang, W., Pákozdi, C., Kamath, A., Martin, T., Bihs, H., 2022b. Hydrodynamic coupling of viscous and non-viscous numerical wave solutions within the open-source hydrodynamics framework REEF3D. J. Offshore Mech. Arct. Eng. (ISSN: 0892-7219) 144 (4), 041903.
Wei, G., Kirby, J.T., Grilli, S., Subramanya, R., 1995. A fully nonlinear Boussinesq model for surface waves. Part 1. Highly nonlinear unsteady waves. J. Fluid Mech. 294, 71–92.

Whalin, R.W., 1971. The Limit of Applicability of Linear Wave Refraction Theory in a Convergence Zone.. Research Report H-71-3, Technial Report, U.S. Army Corps of Engineers.

Zijlema, M., Stelling, G., 2005. Further experiences with computing non-hydrostatic free-surface flows involving water waves. Internat. J. Numer. Methods Fluids 48 (2), 169–197.

Zijlema, M., Stelling, G., Smit, P., 2011. SWASH: An operational public domain code for simulating wave fields and rapidly varied flows in coastal waters. Coast. Eng. 58, 992–1012.